RESEARCH ARTICLE

Society For Biomaterials | WILEY

A bioartificial and vasculomorphic bone matrix-based organoid mimicking microanatomy of flat and short bones

Roberto Toni [1,2,3,4] | Fulvio Barbaro [5] | Giusy Di Conza [5] | Nicoletta Zini [6,7] | Giulia Remaggi [8] | Lisa Elviri [8] | Giulia Spaletta [9] | Enrico Quarantini [4] | Marco Quarantini [4] | Salvatore Mosca [10] | Silvio Caravelli [11] | Massimiliano Mosca [11] | Francesca Ravanetti [12] | Simone Sprio [1] | Anna Tampieri [1]

[1]ISSMC, CNR, Faenza, Italy

[2]Department of Medicine, Division of Endocrinology, Diabetes, and Metabolism, Tufts Medical Center—Tufts University School of Medicine, Boston, Massachusetts, USA

[3]Academy of Sciences of the Institute of Bologna, Section IV—Medical Sciences, Bologna, Italy

[4]Endocrinology, Diabetes, and Nutrition Disorders Outpatient Clinic—OSTEONET (Osteoporosis, Nutrition, Endocrinology, and Innovative Therapies) and Odontostomatology Units, Galliera Medical Center, San Venanzio di Galliera (BO), Italy

[5]Department of Medicine and Surgery—DIMEC, Unit of Biomedical, Biotechnological and Translational Sciences (S.BI.BI.T.), Laboratory of Regenerative Morphology and Bioartificial Structures (Re.Mo.Bio.S.), and Museum and Historical Library of Biomedicine—BIOMED, University of Parma, Parma, Italy

[6]CNR Institute of Molecular Genetics "Luigi Luca Cavalli-Sforza", Unit of Bologna, Bologna, Italy

[7]IRCCS Istituto Ortopedico Rizzoli, Bologna, Italy

[8]Food and Drug Department, University of Parma, Parma, Italy

[9]Department of Statistical Sciences, University of Bologna, Bologna, Italy

[10]Course on Disorders of the Locomotor System, Fellow Program in Orthopaedics and Traumatology, University Vita-Salute San Raffaele, Milan, Italy

[11]II Clinic of Orthopedic and Traumatology, IRCCS Istituto Ortopedico Rizzoli, Bologna, Italy

Abstract

We engineered an in vitro model of bioartificial 3D bone organoid consistent with an anatomical and vascular microenvironment common to mammalian flat and short bones. To achieve this, we chose the decellularized–decalcified matrix of the adult male rat scapula, implemented with the reconstruction of its intrinsic vessels, obtained through an original intravascular perfusion with polylevolactic (PLLA), followed by coating of the PLLA-fabricated vascularization with rat tail collagen. As a result, the 3D bone and vascular geometry of the native bone cortical and cancellous compartments was reproduced, and the rat tail collagen–PLLA biomaterial could in vitro act as a surrogate of the perivascular extracellular matrix (ECM) around the wall of the biomaterial-reconstituted cancellous vessels. As a proof-of-concept of cell compatibility and site-dependent osteoinductive properties of this bioartificial 3D construct, we show that it in vitro leads to a time-dependent microtopographic positioning of rat mesenchymal stromal cells (MSCs), initiating an osteogenic fate in relation to the bone compartment. In addition, coating of PLLA-reconstructed vessels with rat tail collagen favored perivascular attachment and survival of MSC-like cells (mouse embryonic fibroblasts), confirming its potentiality as a perivascular stroma for triggering competence of seeded MSCs. Finally, in vivo radiographic topography of bone lesions in the human jaw and foot tarsus of subjects with primary osteoporosis revealed selective bone cortical versus cancellous involvement, suggesting usefulness of a human 3D bone organoid engineered with the same principles of our rat organoid, to in vitro investigate compartment-dependent activities of human MSC in flat and short bones under experimental osteoporotic challenge. We conclude that our 3D bioartificial construct offers a reliable replica of flat and short bones microanatomy, and promises to help in building a compartment-dependent mechanistic perspective of bone remodeling, including the microtopographic dysregulation of osteoporosis.

[12]Department of Veterinary Medical Sciences, Section of Anatomy, University of Parma, Parma, Italy

Correspondence
Roberto Toni MD, PhD, Academy of Sciences of the Institute of Bologna, Via Zamboni 31, 40126, Bologna, Italy, tel 0039 051 6592190 (Secretariat).
Email: roberto.toni@unibo.it, roberto.toni@unipr.it

1 | INTRODUCTION

A number of studies have shown that decellularized bone matrices exert a powerful in vivo and in vitro inductive action on bone cell adhesion, proliferation, and mineral deposition by either osteoblasts or skeletal osteoprogenitors including mesenchymal stromal cells (MSCs), human embryonic stem cells, induced pluripotent stem cells, and adipose-derived stem cells.[1,2] However, these models may in vitro display functional limitations including insufficient transport of nutrients, oxygen supply and exchange, metabolic waste discharge, and interstitial fluid movements/shear stress in the inner regions of the scaffolds. To overcome this, bioreactor chambers have successfully been used to ensure dynamic perfusion with culture medium to the bone matrix.[1,2] As a result, in situ reconstitution of the original bone marrow (BM) has been obtained in the cancellous compartment, leading to progressive deposition of ECM and provision of molecular cues for survival and regulation of different seeded stem cells/progenitors,[3] up to mimicking the isolated BM or selective BM niches.[4–6]

However, to the best of our knowledge, a flexible microenvironmental three-dimensional (3D) construct for in vitro investigating the bone remodeling in specific bone compartments (cortical vs cancellous) of microanatomically defined bone types is not currently available. Indeed, recent in vitro bone models have focused on a generic 3D space where cellular interactions might take place. These include self-organizing organotypic bone systems able to stay in culture and display mineral deposition for long periods of time,[7–10] and bone organoids based on either bone ECM transformed to an osteoid-inspired biomaterial, to direct osteoblast mineralization and eventual resting state as periosteal lining cells[11] or trabecular bone to host osteoblasts and osteoclasts, promptly responding to microgravity challenges as those occurring in disuse secondary osteoporosis.[12] Usefulness of bone type-directed 3D organoids is also supported by the evidence that in vivo specificity of bone 3D microanatomy and related compartment geometry of blood vessels regulates the microtopography of bone immune cells,[13] favors 3D assembly of BM subcompartments,[14–17] and constraints the transit of immune cells to the cortical and periosteal layers for interaction with osteoblasts and osteoclasts.[13,18,19] In addition, experimental data suggest that a complex 3D spatial logic underlines BM function inside the bone cancellous compartment where structural blueprints of MSCs, vessels, and surrounding stroma emerge as key features of their microtopographic compartmentalization.[20,21]

Therefore, we developed a 3D bioartificial and vasculomorphic bone organoid recapitulating the microanatomy of flat and short bones. We used the decellularized matrix of the adult male rat scapula, implemented with a 3D reconstruction of its intrinsic blood vessels with polylevolactic acid (PLLA), functionalized with rat tail collagen as a surrogate of vascular parietal ECM. As a proof-of-concept of cell compatibility and utility for in vitro studies of osteoinductive properties, we showed the capacity of this 3D organoid to provide an information to seeded rat MSCs influencing the timescale of their skeletogenic fate in dependance on the bone compartment (cortical vs. cancellous), and to favor attachment and survival of mouse MSC-like cells (embryonic fibroblasts) to the reconstructed vascular walls. Presence of in vivo compartment-dependent osteoporotic lesions in the human jaw and tarsus further suggested that a human bone prototype similar to the rat construct could represent a suitable bone microenvironmental assay for studying in vitro compartment-dependent bone remodeling of human MSC in flat and short bones under experimental osteoporotic challenge.

2 | MATERIALS AND METHODS

2.1 | Animals and rat scapula preparation

A total of thirty six 225–250 g (age of 7–8 weeks) Sprague–Dawley male rats (Charles River, Italy) were used, including 12 animals to obtain macroscopic bone samples (scapula), 12 animals to achieve an in situ 3D reconstruction of the intrinsic vascular network of the scapula with injected biomaterial (see specific section below), and 12 animals as BM donors (see specific section below). All animal studies were conducted in accordance with the guidelines of the Institutional Ethical Committee for Animal Use in Research of the University of Parma, and the Italian Ministry of Health (approval code 18/2016-PR), Italy and animal numerosities chosen based on a previous power analysis (see section 2.12) Following deep anesthesia of animals with intraperitoneal (i.p) Zoletil (50 mg/kg), killing was reached by

i.p. Pentothal Sodium (100 mg/kg) and cervical dislocation. Bones (scapulae, rat tail vertebrae) were surgically detached from their muscular and articular ligaments, and were in vitro cleaned of all intrinsic muscles, leaving the periosteum intact. After a quick rinse in phosphate-buffered saline (PBS, 0.1 M, pH 7.4), bones were stored at −80°C until use.

Decellularization was achieved using a modification of a well-established protocol[22] based on preliminary thawing of the frozen bones at 4°C for 24 h, to allow detachment of all cellular structures by thermal shock. The level of removal of contaminating DNA was determined using the CyQUANT® Cell Proliferation Assay Kit (Invitrogen C7026) under manufacturer procedure and a protocol developed by our group for rat tissues.[23] Briefly, male rat tail vertebrae samples were used either as a reference for control (intact bone) or processed for decellularization, to mimic a treated scapula (decellularized bone). Indeed, tail vertebrae are particularly rich in BM with respect to the cancellous layer of the scapula; thus, thorough removal of vertebral DNA represents evidence for an optimized decellularization process to be applied to the scapula. Intact control and decellularized vertebrae were cryodehydrated (Christ ALPHA 2–4 LSC plus) for 24 h using an ad hoc protocol as shown in the Table 1.

Then, the bones were weighed, rapidly immersed in liquid nitrogen (N2), finely grinded in a pestle, and digested in 1 mL of lysis solution (LS) at 56°C for 48 h. The LS was composed by 1 mg/mL proteinase K in 50 mM Tris–HCl pH 7.6 and a protease inhibitor cocktail, made with 1 mM EDTA +1 mM iodoacetamide +10 μg/mL Pepstatin A. A calibration curve was prepared in a 96-multiwell plate using 200 μL serial dilutions (0, 62.5, 125, 250, 500, and 1000 ng/mL) of the lambda bacteriophage DNA in CyQUANT dye solution. The latter was obtained by mixing the working buffer with the CyQUANT® GR dye at 400X supplied by the kit. For analysis, 5 μL of each digested sample (intact control and decellularized tissues) were dissolved in 195 μL of CyQUANT dye solution, and three replicates were prepared for each sample. Analysis of the calibration curve and samples was performed using a Victor 3 V Multilabel Plate Reader (Perkin Elmer) set to the fluorescein protocol (excitation 485 nm, emission 535 nm). For each sample, the amount of DNA was normalized to both the dilution factor and the dry weight of the tissues, and was expressed as ng of DNA/mg of dry tissue.

Decalcification of the decellularized scapula was achieved using a quick calcium removal by immersion of the decellularized bone matrix fragments in a 10% EDTA/PBS (calcium and magnesium-free) buffer 0.1 M pH 7.4 solution at 4°C for a few days, and then rinsing the bone in calcium- and magnesium-free PBS.

2.2 | Intravascular injection of biomaterial

Deeply anesthetized animals (see above) were perfused through the left ventricle and aorta, using a sharp steel catheter and continuous positive pressure for 20 min, as we previously published for perfusion fixation,[24] or via exteriorization of the vascular pedicles of the scapula and intraluminal insertion of a 25-gauge needle, for immediate local injection of the solutions, based on a well-established perfusion methodology developed by our group for in vivo polymeric material delivery.[25–28] Specifically, intravascular blood was removed using a PBS/heparin sodium (10.000 U/L) for 1–2 min at 37°C, followed by 2.5% (w/v), low viscosity PLLA (Purasorb PL10 poly-L-lactide, batch n.1006000576, viscosity = 1.02 dL/g, Purac Biochem, The Netherlands) in methylene chloride (dichloromethane, Mw = 84.93 g/mol, n. 270,997, Sigma-Aldrich), Then, the intravascular PLLA solution was let to polymerize, leaving the injected rat carcass under a ventilated hood for 3–6 h at room temperature (RT). In this manner, forced evaporation of the organic solvent from a closed system like that of intrascapular blood vessels was favored. Finally, scapulae were removed, stored at −80°C, and processed for decellularization (see above) to give rise to a PLLA-injected decellularized organoid. With this procedure, a polymeric crystalline structure of the PLLA lining the inner surface of the walls of the perfused vessels (arteries, veins, and capillaries) was achieved, as confirmed by previous studies using thermogravimetry.[28]

2.3 | Light microscopy

For macroscopic imaging of the scapulae, a Zeiss NAG 80 VA surgical microscope equipped with a Canon 1100 D digital camera was used. For bright-field light microscopy, intact, decellularized, decellularized-decalcified, and rBMSCs-recellularized decellularized-decalcified scapular fragments were initially fixed for 2 h in 2.5% glutaraldehyde–GTA/0.1 M cacodylate buffer (GTA–cacodylate) at RT, cut into smaller pieces, and fixed again in GTA–cacodylate for 24 h at 4°C. Then, samples were rinsed and postfixed in 1% osmium tetroxide, dehydrated in graded series of ethanol, embedded into either London Resin White or Epon 812 at 60°C for 24 or 48 h, respectively, and cut to 1 micron with an ultramicrotome (Ultracut E, Richert-Jung). Sections were then stained with 1% toluidine blue/sodium tetraborate decahydrate, observed with a Nikon Eclipse E 600 microscope, and images captured using a Nikon Dmx 1200 digital camera and a ACT-1 software. Unmineralized bone resulted of variable blue intensity, whereas mineralized bone colored as a dark/brownish area.[29]

TABLE 1 Cryodehydration parameters.

	Loading	Freezing	Principal drying						Final drying		
Time (h:m)	–	0:02	0:15	2:00	2:00	2:00	2:00	2:00	2:00	2:00	10:00
Temp. (°C)	−40.0	−40.0	−20.0	−20.0	−10.0	0.0	10.0	20.0	30.0	40.0	40.0
Vacuum (Mbar)	–	–	0.1	0.1	0.1	0.1	0.1	0.1	0.1	0.02	0.02

Decellularized, PLLA-injected decellularized, and decellularized-decalcified scapulae were studied using an original adaptation of a well-established variable phase dark-field contrast microscopy technique,[30] developed by our group for analysis of biomaterial-perfused bone samples. Specifically, instead of equipping the standard condenser of a Nikon Eclipse E600 light microscope with a light mask having concentric light annuli as requested by variable phase dark-field contrast, a sufficient superimposition of a partial phase-contrast image to a partial dark-field image was achieved by progressively rotating the phase contrast diaphragm, to geometrically interfere with the light beam passing through a dark-field condenser. In this manner, the operator was able to adjust the superimposed images to his need, producing a set of different specimen luminosities and contrasts, and thus, birefringence intensity from crystalline material of variable thickness such as the intravascular polymerized PLLA.

2.4 | Transmission and scanning electron microscopy

For transmission electron microscopy (TEM) intact, decellularized, and decellularized- decalcified scapular fragments were fixed, osmicated, embedded, and cut as reported for light microscopy (see above). Ultrathin sections (70–90 nm) were collected on 200-mesh nickel grids, stained with 3% uranyl acetate and Reynold's lead citrate, and examined with a Zeiss EM109 apparatus. Images were captured using a Nikon Dmx 1200F digital camera and ACT-1 software.

For scanning electron microscopy (SEM), intact, decellularized, PLLA-injected decellularized, PLLA-injected decellularized coated with rat collagen and seeded with cells (see the specific section below), and decellularized-decalcified scapular fragments were initially fixed as reported for light microscopy (see above). Then, fragments were rinsed in cacodylate buffer, cut in smaller pieces, and refixed in GTA–cacodylate for 1 h at RT, dehydrated in graded series of ethanol, immersed in absolute acetone, freeze-fractured with liquid N2 to expose internal portions of cortical and cancellous compartments (except for PLLA-injected decellularized scapulae/collagen-coated and cell-seeded, already fragmented—see the specific section below), and subjected to critical point drying. To exclude possible distortions of the thermoplastic biomaterial during critical point drying, some PLLA-injected decellularized organoids were quickly rinsed in absolute ethanol, freeze-fractured, and criodehydrated (Christ ALPHA 2–4 LSC plus) for 24 h using an ad hoc protocol (see section 2.1). All samples were mounted on aluminum stubs, and metallized for 90 s using gold sputtering, to cover samples with a 60 nm gold film. The preparations were examined using a Philips 501 device coupled to a Nikon Coolpix digital camera for image acquisition.

2.5 | Rat tail collagen preparation and qualitative mass spectrometry characterization

After killing of the animals (see above), rat tails were collected and stored at −80°C until use. Tail collagen was extracted based on an original adaptation of a standard procedure[31]: Briefly, after initial immersion of the tails in 70% ethanol for 30 min, tendons were isolated under an inverted light microscope (Leica DM IL), and rinsed in PBS. Then, tendons were sterilized by immersion in ethanol 100% for 2–3 min, criodehydrated (Christ ALPHA 2–4 LSC plus) for 24 h using an ad hoc protocol (see section 2.1), weighed and solubilized in acetic acid 0.5 M in distilled water for 48–72 h at 4°C in slow agitation; the ensuing solution was ultracentrifuged (Beckman Coulter Avanti J-20 XP) at $14636 \times g$ for 1 h at 4°C, the supernatant was kept, whereas the pellet containing undigested tendons and debris were discharged. This supernatant was further ultracentrifuged at $34957 \times g \times 45$ min at 4°C, the resulting supernatant collected with the presumption to contain a mixture of different collagens, and either sterilized with an antibiotic/antimycotic cocktail (see above) for immediate use or stored at 4°C up to 1 month.

LC-LIT-Orbitrap XL analysis (i.e. HPLC mass spectrometry) was used to characterize the different types of collagen present in the extraction mixture from the rat tail tendons. Initially, 100 μL of 5% extracted collagen solution was diluted in 100 μL of H2O/0.5 M acetic acid mixture, to obtain a 2.5% extracted collagen solution. Then, the collagen mixture was digested with pepsin (50 mg/0.5 mL; Sigma-Aldrich, P0525000) in a 1:50 enzyme: protein ratio, at 37°C for 72 h (pH 2.46). Digestion was stopped with 1 μL NaOH 30%, the sample dried in liquid N2, and 100 μL of 50:50 H2O/acetonitrile mixture was added.

Analysis of the obtained collagen tryptic sequences was carried out as we previously described for rat thyroid collagen.[23] Briefly, a capillary column Jupiter® 5 μm C18 300 A, 150×0.3 mm (Phenomenex), with pre-filtering column at a flow rate of 5 μL/min was used. Elution mixtures included solvent A (0.1% aqueous formic acid, v/v) and B (0.05% formic acid, 100% acetonitrile, v/v). Gradients were set as follows: 5 min with the 2% solution B, then a graded increase of 2% solution B/min for 15 min, cleaning for 3 min with 85% solution B, and column reconditioning for 11 min with 2% solution B. The mobile phase was delivered by a Dionex Ultimate 3000 chromatography system (Dionex Corporation, San Jose, CA, USA) equipped with a 200 vial capacity sample tray. The volume of the injected samples was 5 μL. Identification of m/z values was obtained by mass spectrometry using an LTQ linear ion trap-Orbitrap instrument (ThermoScientific Corporation, San Jose, CA, USA), equipped with ESI interface, and controlled by Xcalibur software. Optimized interface conditions were as follows: ESI (ionization electrospray source) voltage 3.5 kV, capillary voltage 13 V, capillary temperature 275°C, and tube lens 85 V. In the first scan event (full scan), the m/z window was 200–1800 with a resolution of 60,000. The four highest m/z above a threshold of 100,000 counts were selected for collision-induced dissociation (CID) in the ion trap, with normalized collision energy of 35% and collision gas pressure of 2.3×10^{-3} mbar in the collision cell.

2.6 | Data analysis and bioinformatics

As previously reported by our group,[23] protein recognition was achieved through the Proteome Discoverer™ software (Version 1.4)

with SEQUEST as search algorithm. RAW files were processed using 0.1 AMU precursor ion tolerance and 0.5 AMU fragment tolerance. Processed files were then searched against a custom database, in which all known and hypothetical collagen forms, digestion enzymes, and all possible contaminants (e.g. keratin) were considered. Cysteine carbamidomethylation was selected as fixed modification. Confident identification was obtained using stringent filter criteria: DeltaCN was set at 0.1, XCorr versus charge state was set at 1.5 (1+) and 2 (2+). Peptide probability was set at 0.05 (5%). Each spectrum was then manually validated to avoid false positives. To check for any false negative, manual search was performed on some discarded results. To assess targeted peptide uniqueness, BLAST (Basic Local Alignment Search Tool; https://blast.ncbi.nlm.nih.gov/Blast.cgi) analysis was done using the protein–protein BLASTP algorithm, matrix PAM30, Existence = 10 and Extension = 1 Gap Costs, and the "non-redundant protein sequences" database. BLAST search was restricted to the "rat ECM proteins," with coverage ≥20 and scores between 2.5 and 10 (depending on the stringency of the analysis on specific molecules) as acceptable parameters for the proteins found.

2.7 | ATR-FTIR, and rat tail collagen coating of PLLA

Interference in chemical bonds of rat tail collagen caused by solubilizing agents was assessed using Attenuated Total Reflectance–Fourier Transform Infrared Spectroscopy (ATR-FTIR). As a reference, a 2% w/v rat tail collagen at scaling acetic acid molarities (0.5, 1, and 2 M) was analyzed with a Thermo Nicolet 5700 spectrometer equipped with Smart Orbit diamond ATR working in the spectrum range of 4000–400 cm^{-1}.
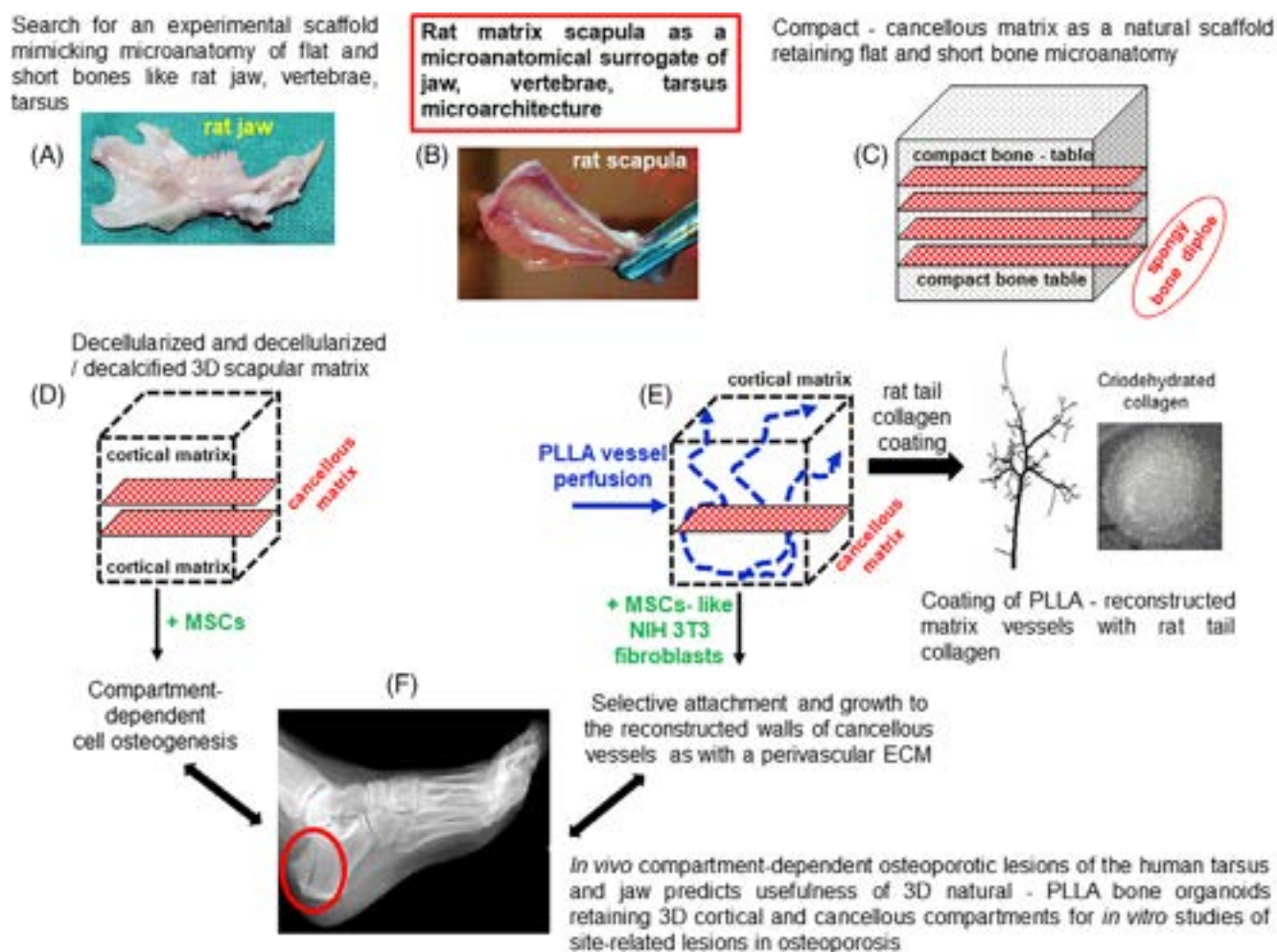

FIGURE 1 Flowchart of the experimental steps to obtain our bioartificial, rat bone organoid. (A) Flat and short bones like jaw, vertebrae, tarsus and, (B) scapula have in common (C) cortical and spongy/trabecular compartments. (D) Decellularization/decalcification was achieved maintaining the 3D microarchitecture of bone compartments. In vitro recellularization with rBMSCs led to a compartment-dependent osteogenesis. (E) Reproduction of the microanatomical organization was increased by reconstructing the vascular walls with an intravascular perfusion of liquid polylevolactic acid (PLLA). Cell compatibility of these vascular walls was favored by their coating with rat tail collagen. As a result, MSC-like cells (mouse embryonic fibroblasts) were in vitro able to grow and attach to them. (F) Finally, in vivo evidence of compartment-dependent selectivity of osteoporotic lesions in the human jaw and tarsus suggested need of a 3D human bone organoid similar to the 3D rat bone organoid to mimic flat and short bones, and to in vitro investigate site-specific effects of experimental osteoporosis.

Changes in the number and type of chemical bonds in the collagen solution were used to verify the chemical stability of the biomaterial.

Coating of PLLA-injected vessels started with sterilization of a 1% w/v solution of rat tail collagen in 1 M acetic acid by chloroform vapors at 4°C overnight; specifically, pure chloroform in a volume equal to about 10% of that of collagen was dispensed at the bottom of a collagen phase, passing through it with the tip of a sterilized Pasteur pipette. It resulted in two liquid phases, where the tail collagen remained above and was eventually collected. Then, coating of the intraosseous PLLA-reconstructed vessels was achieved by immersing the freeze-fractured organoids (see above) in sterile collagen for 5 min, thus allowing collagen deposition and attachment by capillarity to the walls of the exposed vascular branches. Organoids were drained by gravity onto sterilized absorbent paper, and left to dry overnight inside a 24-well plate, under UV light in a laminar flow hood. To stabilize PLLA-collagen interactions, some organoids were criodehydrated (Christ ALPHA 2–4 LSC plus) for 24 h using an ad hoc protocol (see section 2.1). Then, organoids were placed in a 2% penicillin/streptomycin (P/S) solution containing 40 μL/100 ml gentamicin, kept overnight under UV light, rinsed with culture medium, and seeded with cells.

To assess the 3D microgeometry of the collagen coating after criodehydration, four independent 2% w/v rat tail collagen preparations in 1 M acetic acid were layered on the surface of polymerized PLLA disks[32] retaining the same surface geometry observed in PLLA-perfused vessels.[28] Then, these samples were cryodehydrated (see section 2.1), prepared for SEM (see details at section 2.4), with all images acquired at the same magnification (160X), and analyzed using AxioVision 4.8 image analysis software (Zeiss). In each sample, 20 interfibrillar spaces (i.e. micropores) were randomly selected, and their surface area calculated by manually tracing the edges of each micropore with a graphic cursor. At the end of the tracing, the software returned the surface area measurement ($μm^2$).

2.8 | Isolation of rat BM stromal cells (rBMSCs) and culture splitting assessment

rBMSCs were isolated as we recently reported.[32] Briefly, the femur BM of killed animals was collected by inserting an 18-gauge needle into the bone diaphysis and, under sterile conditions flushing it into a sterile Petri dish with DMEM low glucose (LG) containing 10% fetal calf serum (FCS), and an antibiotic–antimycotic combination of 100 μg/mL penicillin, 10 mg/mL streptomycin, and 25 μg/mL amphotericin B (Euroclone, Italy). This solution was used as a
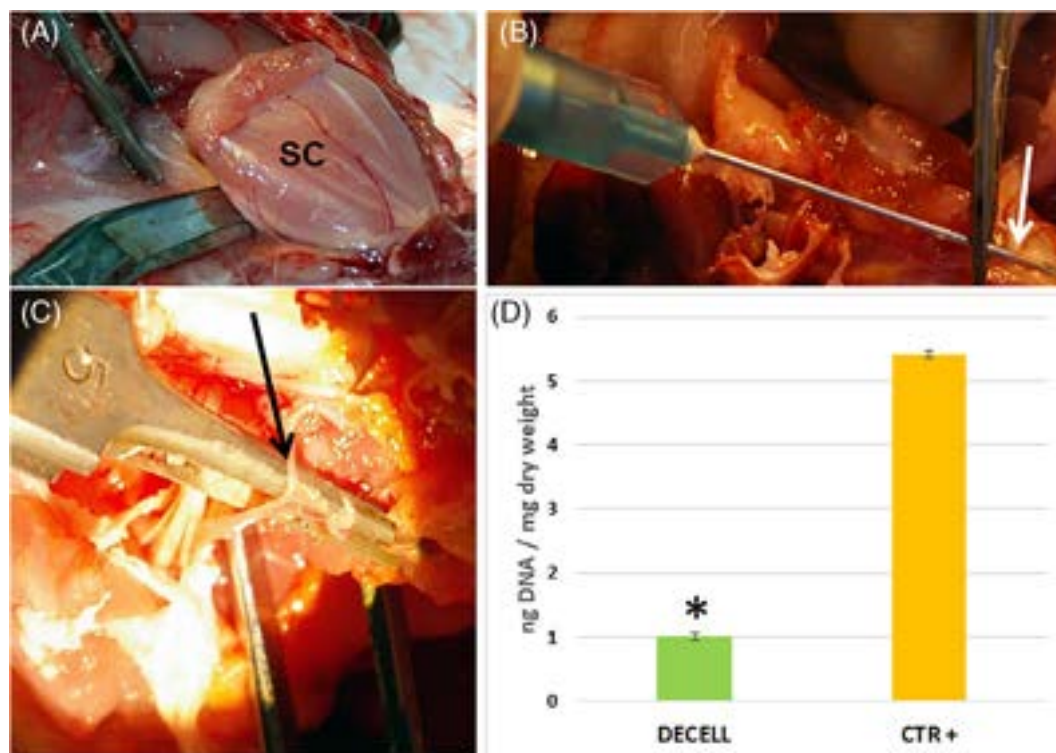

FIGURE 2   Main methodological steps for preparation of the rat bone scapular matrix. (A) Anterior–posterior exteriorization leaving the subscapular muscles in situ, eventually removed *en bloc* before detachment of the bone from its articular ligaments; (B) reconstruction of intrinsic scapular vessels by intravascular injection of polylevolactic acid (PLLA). After in situ exteriorization of a scapular vascular pedicle (arrow) (C), its direct cannulation was pursued with a fine needle (arrow) allowing for immediate access of the biomaterial solution to the intraosseous vascular network; (D) amount of DNA in control and decellularized male rat vertebrae, as determined by CyQUANT analysis. A statistically significant reduction of more than fivefolds (asterisk) in DNA occurred in decellularized (DECELL) compared to control (CTR) bones. Each bar represents the mean ± SD of the three separate experiments, *p < .0001.
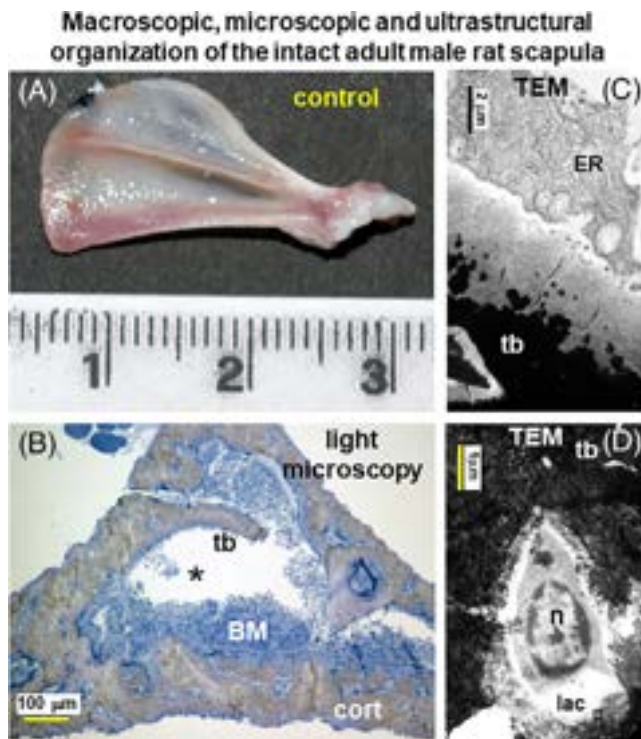
FIGURE 3 Control scapula. (A) macroscopic image; (B) light microscopic section. Cort = cortical bone compartment; tb = trabecular bone compartment; BM = bone marrow, in the spongy cavity (asterisk); (C) TEM of a control cancellous trabecula (tb), highly electrondense (black color) as a result of mineralized matrix. This is covered by a 8–10 microns thick amorphous layer of collagen, supporting a bone cell (likely an osteoblasts) with well-developed endoplasmic reticulum (ER); (D) TEM of a black electrodense mineralized trabecula (tb) entrapping an osteocyte with evident nucleus (n) in an osseous lacuna (lac). Sizes of all makers are depicted in the images. Each image represents the result of a sample selected from an average of three different experiments.

culture medium. Then, BM mononuclear cells were isolated by gradient centrifugation on Histopaque-1077 (Sigma-Aldrich), washed twice in culture medium, counted in a Burker chamber, and plated on a standard plastic T25 flask (Corning, USA) at a density of $2 \times 10^5/cm^2$. After 72 h, nonadherent cells were removed, adherent cells reseeded in a T25 (passage 0 or P0), and the medium replaced every 2–3 days. At 80% confluence (i.e. subconfluence), cells were detached using trypsin 0.02% EDTA for 1 min, splitted 1:2, reseeded, cultured with the same procedure up to complete passage 2 or P2, and then used for all experiments. Consistency in the morphology of rBMSCs during the P0–P2 interval was checked using an inverted, phase-contrast light microscope (Zeiss Observer A1).

Since we had previously determined the replicative efficiency (cell doubling and doubling time) of male rBMSCs in the P0–P2 interval,[32] we only estimated the proportion of cells present in culture at each passage, as an indication of consistency of cell growth in a culture interval retaining the highest differentiation potential.[33] To achieve this, we designed an iterative procedure dependent on the initial

number of culture flasks, assuming that: (a) cell behavior was identical in each flask; (b) in each flask, cells reached the same subconfluence, that is, 80% occupancy of the flask surface; (c) subconfluences related to a specific passage were attained within the same time end point. These assumptions were considered feasible based on previous evidence that in the same cell system, proportion between cell subtypes (large and small cells) remained constant at different culture passages, no flask was lost during the entire 1:2 splitting procedure, and the overall cell content was splitted uniformly.[32] For this purpose, we used the following equation:

$$F_k = \left(2^k\right) \times F_o$$

where F_k was the number of flasks at the k-th culture passage, F_o was the initial number of flasks, and k the specific culture passage.

2.9 | Flow cytometric immunophenotyping

At P2, rBMSCs in standard flasks were trypsinized, centrifuged at $220 \times g$ for 10 min, resuspended in culture medium, and counted using a Burker chamber. A solution of 7×10^4 cells in 100 μL of a PBS buffer containing 0.1% sodium azide and 2% fetal bovine serum (FBS) was used for each flow cytometric point, as we previously reported.[32] Briefly, cells were incubated at 4°C for 15 min with monoclonal antibodies against rat CD45, CD73, CD90 (BD Pharmingen, USA), and their isotype controls (IgG2a, Abcam, UK) at a concentration of 1:20. Then, samples were washed with buffer, centrifuged, resuspended in the same buffer, and incubated with FITC-labeled secondary antibody (1:20, Dako, USA) for 15 min in the dark at RT. After a final wash, the cells were analyzed using a Becton Dickinson FACS-Canto II, equipped with a blue laser capable of detecting light scattering. The FITC fluorescence was filtered by a 530 ± 21 nm bandpass filter. A single gate was applied on the forward versus side scatter, to allow selection of the suitable cell population. The frequency of positive cells was measured as the percentile of cells gated in the FITC channel with activities above 99.0% of the corresponding isotype control. Data were analyzed with the FACSDIVA software (Becton Dickinson).

2.10 | Organoid recellularization with rBMSCs and Swiss 3T3 fibroblasts

At P2, rBMSCs were grown in T25 plastic flaks until 80% subconfluence, detached by trypsin 0.02% EDTA for 1 min, and dropped at $140 \times 10^3/cm^2$ onto a decellularized-decalcified scapular organoid fixed with biocompatible and sterile dental glue to the bottom of a culture well. After 30 min in incubator, cell culture medium (DMEM-LG/ FCS/antibiotics–antimycotics, see above) was added, and changed every 48 h up to 43 days. After 24 h of cell adhesion, some cultures were differentiated using an osteogenic medium (DMEM-LG/50 μM ascorbic acid/10 mM alpha-glycerol
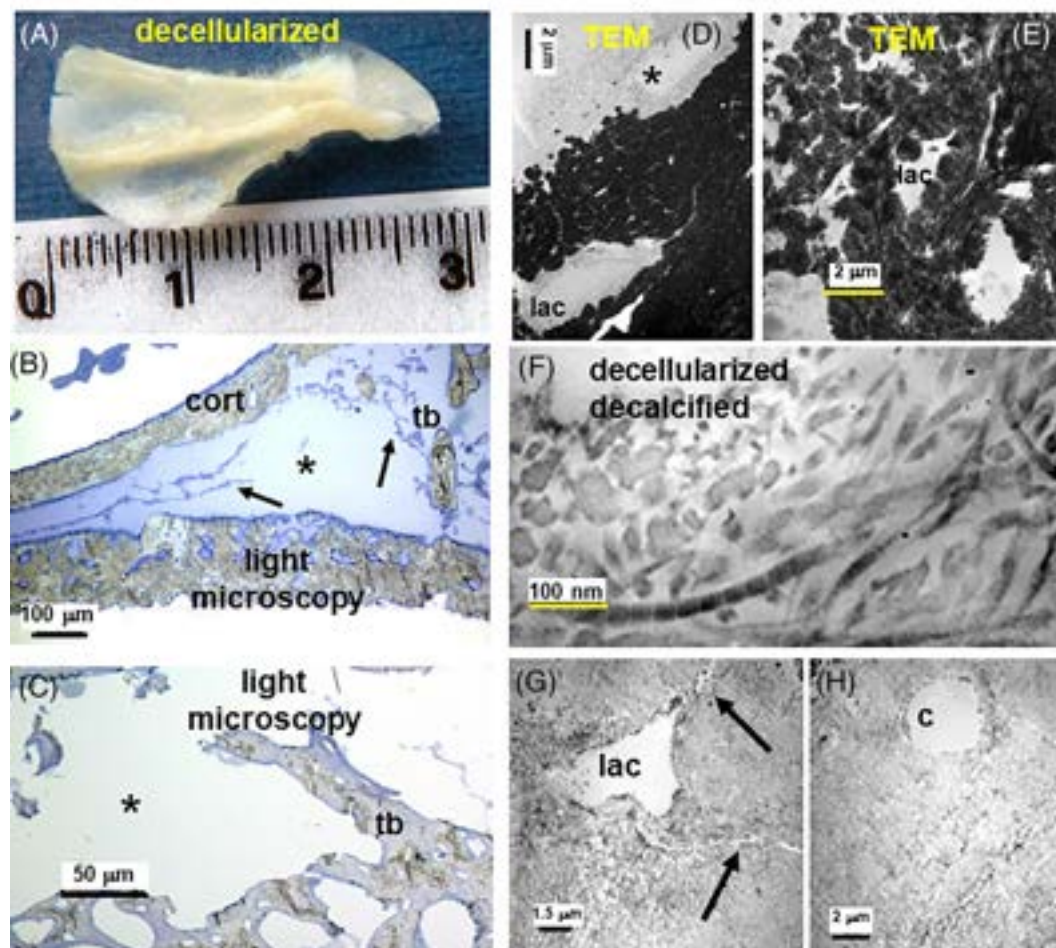
FIGURE 4 (A) Decellularized scapula; (B,C) light microscopy of decellularized scapular matrix. (B) The asterisk highlights complete absence of BM cells in the cancellous cavity, but retainment of the blue reticular BM stroma (arrows), and the connective periosteal and endosteal layers; (C) trabecular bone (tb) with empty osteocyte lacunae; (D,E) ultrastructure of a decellularized, cancellous trabecula with mineralized matrix (black color), numerous empty osteocyte lacunae (lac) with canaliculi, and D) an osteoblast site (asterisk) in the trabecular collagen layer (amorphous material); (F–H) ultrastructure of decellularized – decalcified, trabecular fragments showing F) collagen fibrils with the typical banding, and (G,H) collagen matrix devoid of bone mineral, but retaining empty osteocyte lacuna (lac) with canaliculi (arrows) and profile of a blood capillary (c). Sizes of all makers are depicted in the images. Each image represents the result of a sample selected from an average of three different experiments.

phosphate/0.1 μM dexamethasone), replaced every 48 h up to 43 days. Deposition of ECM, vesicular release, and signs of mineralization were assessed at 7, 21, and 43 days, using light microscopy and SEM analysis (see above). In addition to standard cell seeding, enhancement of cell attachment to the decellularized-decalcified scapular organoid was also tested by cultivating rBMSCs in dynamic bioreactor-like conditions. Specifically, cells at P2 were dropped directly into the medium of each growing well (6-well plate) containing a bottom-fixed 3D organoid, and each plate was subjected to 15–30 min of horizontal rotation coupled to oblique tilt (five cycles per min) using a sterile and temporized agitator inside the cell incubator. Following either passive or dynamic cell seeding, cell attachment to the organoid was checked using an inverted, phase-contrast light microscope (Zeiss Observer A1).

To test the capacity of the PLLA-rat tail collagen complex to favor attachment and growth of MSC-like cells, NIH Swiss 3 T3 murine embryonic fibroblasts (courtesy of Prof. Lucio Cocco, University of Bologna, Italy) were grown at 10×10^3 cells/cm^2 for 72 h onto the rat tail collagen-PLLA complex. DMEM high glucose (Euroclone ECB7501L) with 10% FBS (Aurogene AU-S1810), 1% essential amino acids (Aurogene AU-X0557), 1% glutamine (Aurogene AU-X0550), 1% P/S (Aurogene AU-L0022), and 20 μL/100 mL gentamicin (Sigma Aldrich G1397) was used as a medium. Cell attachment was analyzed by SEM (see above).

2.11 | Human subjects, and densitometric/ radiographic/surgical studies

A sample of 28 subjects (age range: 21–81 years; female to male ratio 3:1; body mass index range 21.5–35.8 kg/m^2) was randomly extracted from routine outpatients of endocrine-metabolic and

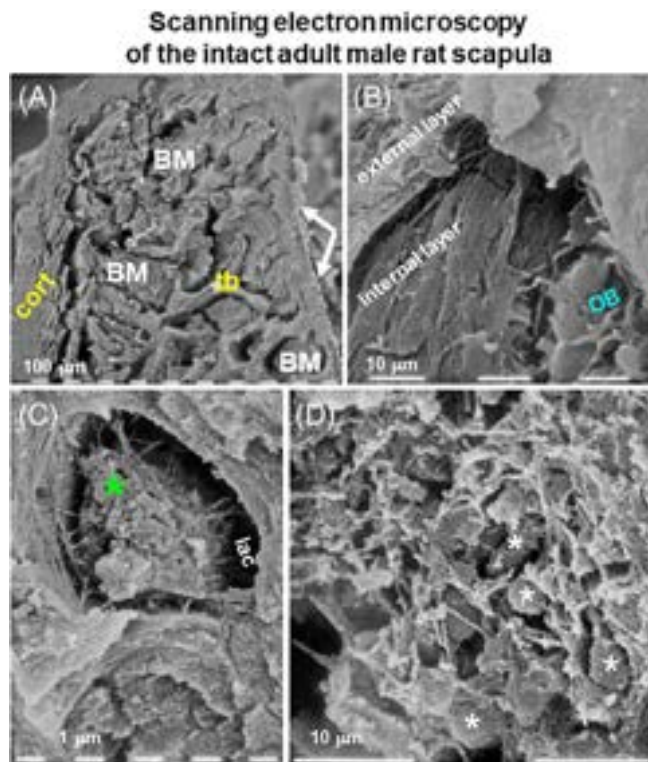## Scanning electron microscopy of the intact adult male rat scapula

FIGURE 5 SEM of control scapula. (A) cortical (cort) and trabecular (tb) compartments retained the periosteum (white arrows) and BM and, (B) the periosteum displayed two layers with osteoblasts (OB), whereas (C) an osteocyte (green asterisk) is visible inside a lacuna (lac) of the cortical compartment; (D) BM cells (white asterisks) remained enveloped in the reticular stroma of the cancellous cavity. Sizes of all makers are depicted in the images. Each image represents the result of a sample selected from an average of three different experiments.

odontostomatology clinics (OSTEONET and Odontostomatology Units, Galliera Medical Center—GMC, Italy). Exclusion criteria were cancer and known clinical conditions of secondary osteoporosis. Dual-energy X-ray absorptiometry, magnetic resonance imaging and, when appropriate surgical evaluation were retrospectively collected to assess bone mass density levels in standard sites (lumbar column, femur), and topography of cortical versus cancellous lesions in selected sites (jaw, foot tarsus). All data were used following approval by the GMC Ethical Committee, and under patient's informed consent omitting any case-sensitive information.

2.12 | Statistical analysis

The sample sizes of the animal studies for organoid recellularization and reconstruction of intrinsic vascular network were calculated using the G*Power v.3.1.7 software (Franz Faul, Universität Kiel, Germany). By considering an obtained effect size ($d = 1.78$) with a power of 80% and a value of $p < .05$, we predicted an effect size $f = 0.50$ leading to a minimum of $n = 6$ animals/group (three-way

ANOVA for repeated measures). In addition, differences were considered in: (a) nanogram of DNA/milligram of dry weight between controls and decellularized rat tail vertebrae; (b) number of flasks containing rBMSCs at each culture passage; (c) number of days to reach subconfluence of rBMSCs at each culture passage; (d) surface area of micropores between different preparations of dehydrated rat tail collagen. These differences were evaluated using a one-way ANOVA and Student t tests on means, and were considered significant if $p < .05$.

3 | RESULTS

3.1 | Steps for engineering the bioartificial bone organoid

A number of preparation steps were pursued to reliably in vitro engineer a rat, 3D bone construct recapitulating the microanatomical architecture common to rat flat and short bones like the jaw, vertebrae, and tarsus. Figure 1 shows the flowchart of this experimental approach; all flat and short bones including the scapula have in common a compact bone layer (cortical compartment), acting as a cortex surrounding a spongy/trabecular bone core (cancellous compartment), acting as a reservoir of BM. Removal of all cells and mineral hydroxyapatite (decellularization/decalcification) without distortion of the 3D bone scapular microarchitecture resulted in a 3D stromal/fibrous matrix deprived of the walls of its intrinsic vessels. In vitro recellularization of this 3D bone "ghost" with rBMSCs led to a compartment-dependent osteogenesis, confirming cell compatibility and osteoinductive properties of the native stromal microenvironment.

Since both cancellous and cortical compartments of the bone organoid are transversed by vessels acting as conduits for bone cell trophism and intraosseous cell transit, in parallel experiments, we increased the microanatomical similarity between the engineered organoid and a native stromal-vascular matrix of a flat and short bone. To achieve this, we reconstructed the cancellous and cortical vascular walls with an intravascular perfusion of liquid polylevolactic acid (PLLA), let to polymerize inside the native bone before its decellularization/decalcification. Cell compatibility of these vascular walls was favored by coating their external surface with rat tail collagen, acting as a surrogate of the native perivascular ECM. As a result, in vitro growth and attachment of MSC-like cells (mouse embryonic fibroblasts) to the reconstructed vessel walls readily occurred. Finally, to get some hints on the most suitable organoid for in vitro studying the behavior of human MSCs in osteoporotic flat and short bones, we in vivo searched for osteoporotic lesions in the human jaw and foot tarsus. We obtained evidence for a selective involvement of either cortical or cancellous compartments. We concluded that a 3D human bone organoid recapitulating the 3D microanatomy of cortical and cancellous compartments, as our 3D rat model, would represent an ideal microenvironmental assay for in vitro studying the response of human MSC to an osteoporotic challenge in flat and short bones.
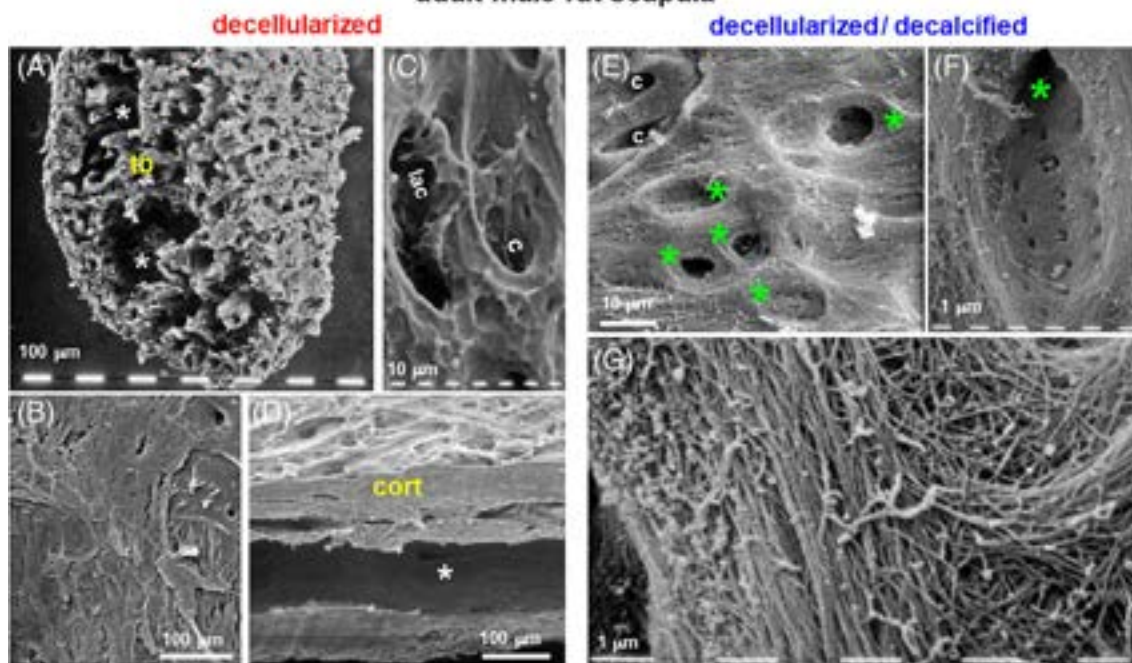
FIGURE 6 SEM of decellularized, and decellularized-decalcified scapular matrix. (A) cancellous trabeculae (tb) of the scapular blade intermixed with empty BM spaces (white asterisks); (B) connective fibers of the periosteal layer; (C) empty osteocyte lacuna (lac) in the compact bone, c = blood capillary canal; (D) cortical layers (cort) of the scapular spine bordering its empty central space (white asterisk); (E) empty osteocyte lacunae (green asterisk) and blood capillary canals (c) in the homogeneous fibrous matrix of the cortical layer; (F) osteocyte lacuna (green asterisk) revealing circumferential fibers at its contour, dense woven fibers on the walls and floor, and holes of the osteocyte canaliculi; (G) variably oriented (parallel, orthogonal, reciprocally intersecting, arching) groups of collagen fibrils constituting the compact bone matrix. Sizes of all makers are depicted in the images. Each image represents the result of a sample selected from an average of three different experiments.
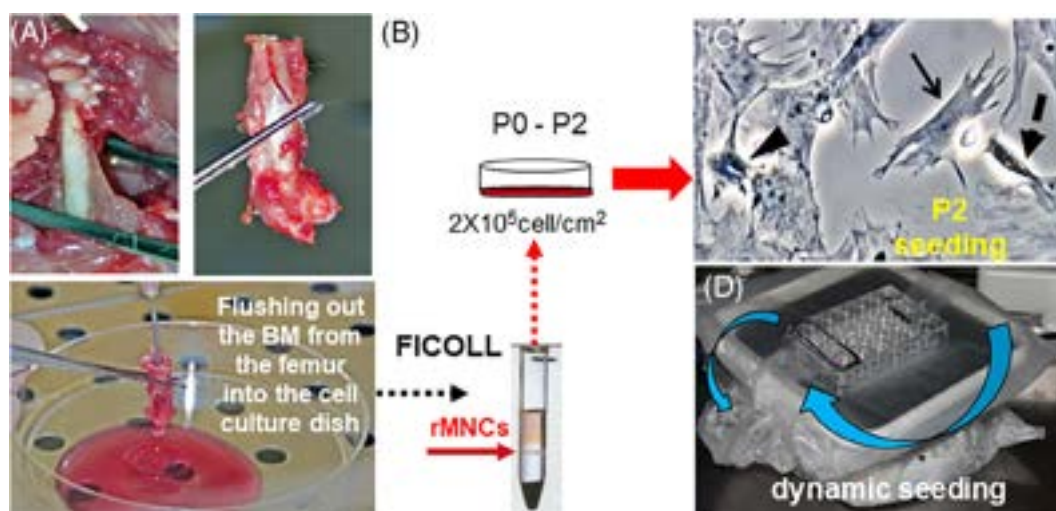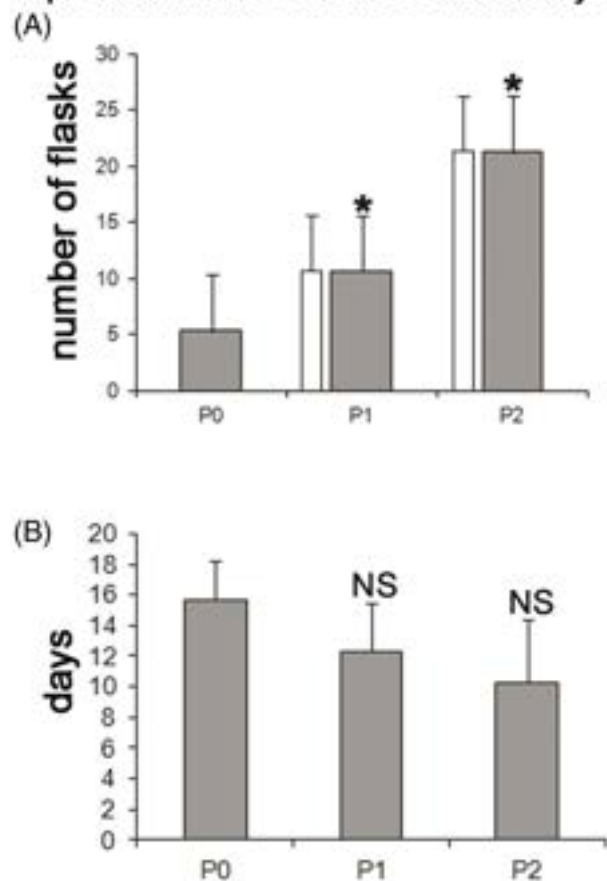

FIGURE 7 Schematics of the procedure for isolation and culture (either static or dynamic) of rBMSCs. (A) Cells were recovered from the BM of the femur, and (B) mononuclear types (rMNCs) isolated (small red arrow) by density gradient and expanded at low concentration in monolayers, up to the second culture passage (P2); (C) as predicted by our previous studies and confirmed by current analysis at the inverted phase-contrast light microscope (40×), rBMSCs included small fibroblast-like (dotted arrow), polygonal (arrowhead), and large flattened (arrow) cells at any culture passage, here exemplified at P2; (D) rotation-tilt (blue arrows) agitator suitable for adaptation inside the incubator chamber and used to achieve, in some experiments, a dynamic seeding in the presence of the bone organoid (see technical details in Materials and Methods).
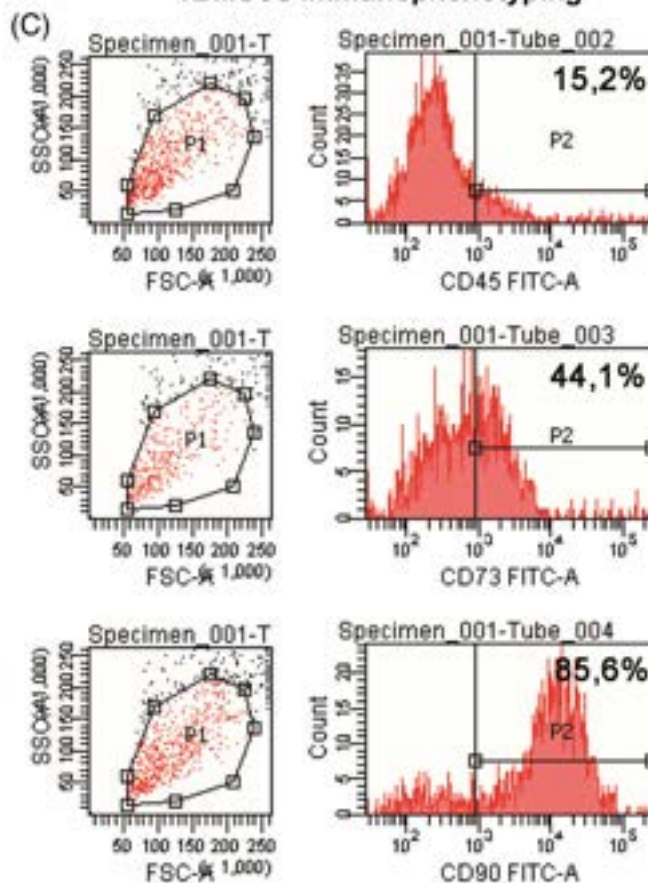
FIGURE 8 Kinetics of rBMSCs expansion and their immunophenotyping. (A) Between P0 and P2, a statistically significant increase occurred in the mean number of flasks (dark bars) containing 80% subconfluent cells. This trend was confirmed by a theoretical cell splitting analysis (white bars, see Materials and Methods for details) based on assumption of cell homogeneity in each culture flask. (B) In the same culture intervals, no statistically significant difference was observed in mean number of culture days to reach subconfluence at each passage, as expected for constancy in the cell replication rate. Bars represent the mean ± SD of three separate experiments, *$p < .00001$; NS = not significant ($p = .15$); (C) flow cytometric immunophenotyping confirmed prevalence of CD90-, and CD73-positive cells as opposed to CD45 cells, whereas scatter plots revealed constancy in distribution of cell size and granularity, reflecting constancy of three cellular phenotypes. Each graph represents the result of the same index experiment.

3.2 | Scapular matrix and its biomaterial perfusion

Figure 2 shows the main technical steps of the original surgical procedure we developed for isolation of the rat scapula and biomaterial injection of its intrinsic vessels, as well as the quantitation of residual DNA following decellularization. Scapulae were surgically removed using anterior–posterior approach to avoid damage of the subscapular muscles and related periosteum, the former eventually detached *en bloc* before the bone was made free from its articular ligaments, while keeping the latter intact. However, to achieve the reconstruction of the intrinsic scapular vessels, the scapulae were initially left in situ, and intravascular injection of a solution of PLLA was performed through scapular vascular pedicles, allowing for biomaterial solution to perfuse the entire intraosseous vascular network. Once the entire 3D scapula was decellularized, quantity of cell removal was assessed by analysis of residual DNA, resulting in a statistically significant reduction

(more than fivefolds) in DNA amount in decellularized compared to control bones.

Results of the structural quality of the scapular matrix preparation in comparison to controls are summarized in Figures 3–6. In particular, Figures 3 and 4 detail the macroscopic morphology, light microscopic architecture, and transmission electron microscopic (TEM) ultrastructure of control, decellularized, and decellularized/decalcified rat bone scapulae. Figure 3 shows that control cortical and trabecular bone compartments exhibited toluidine blue-stained, periosteal and endosteal connective layers, and BM cells in the cancellous spaces. Similar, Figure 4 shows that the decellularization procedure allowed for maintenance of a "ghost" matrix of the entire 3D scapula, with a 3D morphology identical to that of the control bone. At the light microscopic level, decellularized scapulae showed a well-preserved 3D architecture of the periosteum, endosteum, trabecular and cortical compartments, but complete deprivation of BM, osteoblasts,
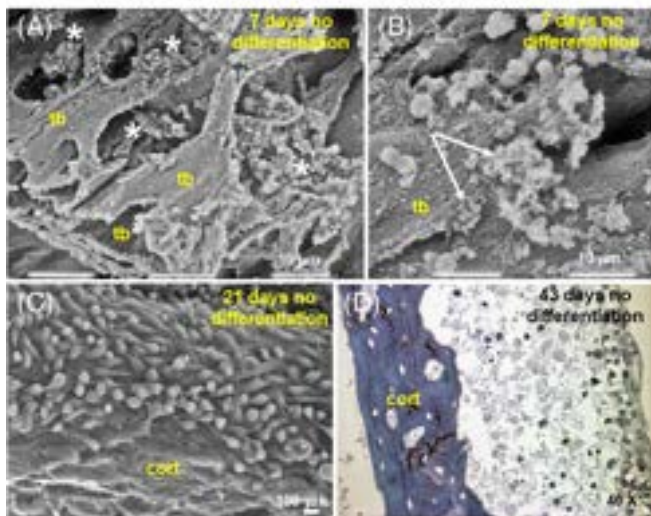
FIGURE 9 SEM and light microscopy of decellularized-decalcified scapular matrices recellularized with rBMSCs without osteogenic medium. (A) After 7 days of standard culture, the cells colonized the empty intertrabecular (tb) spaces of the cancellous compartment organizing in insulae (white asterisks) (B) immersed in a reticular/flocculent substance (white arrows), consistent with neosynthesized ECM; (C) After 21 days, the seeded cells were actively growing filling the surface of the cortical matrix and, (D) after 43 days, cells (dark nuclei) accumulated over the matrix of the cortical (cort) compartment with no evidence of mineral mass deposition (maintenance of a blue color in the collagen fibers, devoid of mineralized brown material). No differences were observed when dynamic seeding was applied. Optical enlargement and/or sizes of all makers are depicted in the images. Each image represents the result of a sample selected from an average of three different experiments.

osteoclasts, and lacunar osteocytes. TEM of these preparation confirmed presence of cancellous trabeculae with a well-mineralized matrix, but empty osteocytes lacunae and loss of osteoblasts in the trabecular collagen layer. TEM of decellularized-decalcified fragments of the scapular trabeculae revealed that the decalcification process did not hamper their fibrous organization, leaving the demineralized matrix as a compact and regular structure of collagen bundles with typical orthogonally oriented banding of the collagen fibrils, empty osteocyte lacunae, and spaces for blood capillary.

Finally, adequate bone matrix preparation was highlighted at the scanning electron microscopic (SEM) level. In Figure 5, control scapulae exhibited cortical and trabecular compartments, two layers of periosteum, and BM. In the cortical bone, osteoblasts were present in the periosteum, and osteocytes occupied lacunae, whereas BM cells remained enveloped in the reticular stroma of the cancellous cavity. In contrast to controls, in Figure 6, decellularized scapular matrix revealed cancellous trabeculae with empty BM spaces, whereas cortical layer was devoid of cells in osteocyte lacunae and blood capillaries, though the periosteum remained intact. Finally, in the decellularized-decalcified scapular matrix, the cortical layer contained profiles of blood capillaries and empty osteocyte lacunae immersed in a

homogeneous fibrous matrix. The contour of the lacunar spaces was made of circumferential fibers, whereas dense woven fibers formed the lacunar walls and floor. Collectively, the compact bone matrix was made up of different layers of variably oriented (parallel, orthogonal, reciprocally intersecting, arching) groups of collagen fibrils, ensuring conservation of the 3D microarchitecture of the cortical layer.

3.3 | rBMSCs isolation, growth, immunophenotyping, and their matrix recellularization

Figure 7 schematizes the procedure for isolation and culture of rBMSCs. Cells were obtained from the BM of the femur, mononuclear types collected through density gradient and, to preserve their differentiation potential expanded in standard monolayers up to the second culture passage (P2). Consistent with our previous studies,[32] at all culture passages (P0–P2) inverted phase-contrast light microscopy revealed three cell phenotypes including small fibroblast-like, polygonal, and large flattened cells (Figure 7C). In some experiments of organoid recellularization (see below), the cells were grown in dynamic seeding using a rotation-tilt equipment, with the intent to speed up the process of cell attachment to the bone matrix.

As summarized in Figure 8, replication stability of all mononuclear cell phenotypes was confirmed at 80% subconfluence, showing a statistically significant increase in the total number of cells at each split, also when theoretically constrained by the assumption of cell homogeneity. Consistently, no statistically significant difference was observed in the mean number of culture days to reach subconfluence at each passage, suggesting constancy in cell replication rate during each culture interval. Finally, flow cytometric analysis revealed a percentage of CD45-, CD73-, and CD90-positive cells consistent with an immunophenotype typical for BMSCs of a strain and age of rats as we used, and of P2 subculture passage. Retainment of homogeneity in cell phenotypes was also supported by the constancy in distribution of cell size and granularity at forward and side scatter analysis (Data courtesy of Alessandra Zamparelli, Grant FIRB RBAP10MLK7_004 postdoctoral Fellowship 2010–2015, UNIPR, Parma, Italy and Luca Cattini, Laboratories of Immunorheumatology and Tissue Regeneration, RAMSES, IOR, Bologna, Italy).

Microtopographic compartmentalization and related temporal activation of rBMSCs seeded onto a decellularized-decalcified bone organoid are highlighted in Figures 9 and 10. After 7 days in culture without any differentiating agent, SEM revealed that cells primarily aggregated in insulae onto the surface of cancellous trabeculae, in strict adhesion to the fibrous matrix, surrounded by a reticular material consistent with ECM (Figure 9). This behavior was consistent with rBMSCs committed to a skeletogenic lineage, and de novo secreting interstitial proteins/basal membrane. In contrast, only after 21 days SEM showed that cells progressively colonized the surface of the cortical compartment but without evidence of ECM deposition and/or release of matrix vesicles (Figure 9). This suggested a selective influence of the cancellous versus cortical stromal matrix in inducing rBMSCs to a skeletogenic lineage. However, when these cells were

FIGURE 10 SEM and light microscopy of decellularized-decalcified scapular matrices recellularized with rBMSCs and osteogenic medium. (A,B) rBMSCs cultivated for 21 days in standard culture showed colonization of the cancellous trabeculae (tb), and release of matrix vesicles (300–1000 nm in size) for mineralization (yellow arrows); (C) after the same time interval, the cortical matrix revealed progressive cell colonization (black arrows) inside the compact bone compartment, but absence of mineral deposition; (D) only after 43 days, rBMSCs gave rise to a thick layer of dark brownish mineral mass (MM) on the surface of the cortical (cort) matrix, whose unmineralized collagen layer remains of blue color. No differences were observed when dynamic seeding was applied. Optical enlargement and/or sizes of all makers are depicted in the images. Each image represents the result of a sample selected from an average of three different experiments.
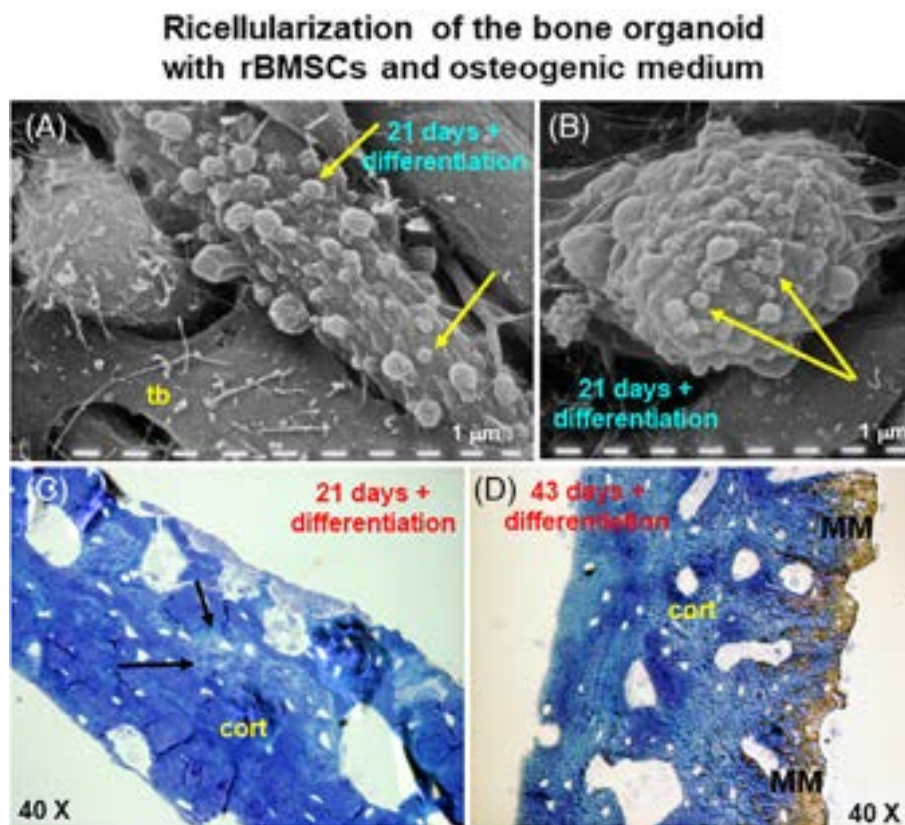
induced to osteogenic differentiation for 21 days, they actively deposited mineral mass and released typical matrix vesicles (300–1000 nm in size) within the fibrous scaffold of both compact and cancellous compartments, as determined by SEM and light microscopy (Figure 10). Confirmation of a different microtopographic regulation of seeded rBMSCs was obtained after 43 days of culture; rBMSCs growing without any differentiation continued to accumulate within the cortical compartment but in the absence of mineral mass deposition (Figure 9). In contrast, rBMSCs induced to osteogenic differentiation gave rise to a thick cortical layer of mineral mass (Figure 10). Finally, the use of dynamic seeding by a rotation-tilt equipment during initial cell growth favored cell attachment to the decellularized-decalcified organoid, allowing a faster stabilization of the rBMSCs microtopographic compartmentalization, although it did not change the osteogenic differentiation timescale with respect to standard static seeding (recellularization experiments courtesy of Alessandra Zamparelli, Grant FIRB RBAP10MLK7_004 postdoctoral Fellowship 2010–2015, UNIPR, Parma, Italy).

3.4 | Vascular reconstruction with PLLA and PLLA coating with rat tail collagen

The accuracy of the microscopy technique used to visualize the PLLA lining of vessels in the scapular matrix is shown in Figures 11 and 12. In the absence of PLLA injection, and regardless the type of scapular matrix preparation (either decellularized or decellularized/decalcified),

Figure 11 shows that no differences in luminosity/color were observed inside and outside the cortical vascular canals, confirming that their visualization with either bright-field or variable phase dark-field contrast light microscopy was not altered by the presence or absence of mineralized mass.

In contrast, Figure 12 shows that the crystalline structure of PLLA lining the walls of intraosseous blood vessels in the perfused, decellularized scapular cortex produced a light-blue birefringence, as observed using the variable phase dark-field contrast light microscopy ad hoc developed for these studies (see Materials and Methods for details). This was consistent with the white color of the biomaterial observable with single phase-contrast light microscopy. Similar, SEM analysis of the decellularized cancellous compartment revealed biomaterial-dependent, 3D reconstitution of tufts of blood vessels and fine capillaries/sinusoids in the intertrabecular spaces, where the BM cells usually reside.

The molecular composition of the rat tail collagen prepared for coating PLLA-reconstructed vessels is summarized in Figure 13. Qualitative mass spectrometry analysis (LTQ-Orbitrap XL) showed that it was a mixture of numerous collagen types and subtypes whose main components were collagen 1 and 3, typical of the bone ECM. Chemical stability of the collagen solution was evaluated by ATR-FTIR spectroscopy. Figure 14 shows that dilution of the collagen mixture with standard solvents (acetic acid) in a 0.5–2 M concentration range did not modify number and type of its chemical bonds, thus leading to spectroscopic peaks almost identical in each of the three tested conditions. This confirmed structural reliability
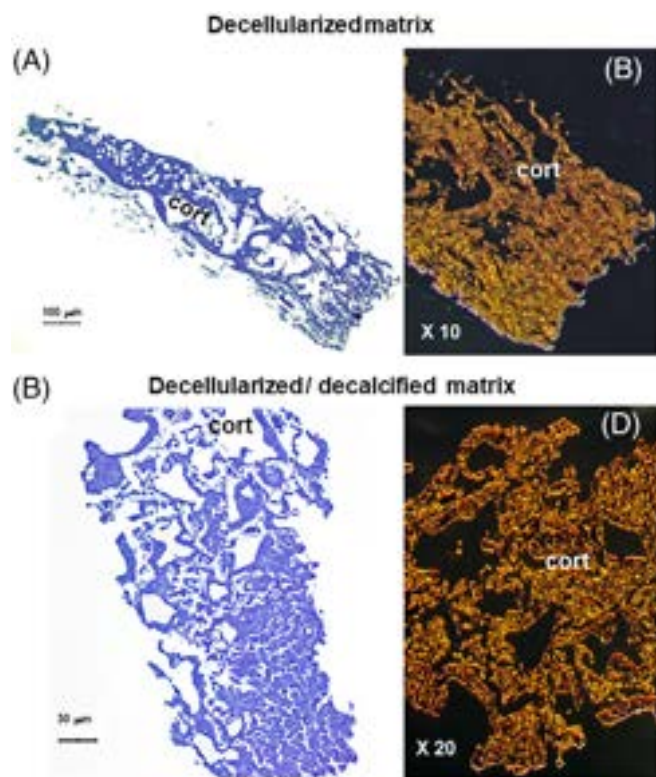
FIGURE 11 Variable phase dark-field contrast (VPDFC) light microscopy (A) Decellularized cortical compartment (cort) of the scapular matrix, stained with toluidine blue and visualized by bright field; (B) a similar preparation observed using VPDFC; (C) decellularized–decalcified cortical compartment (cort) of the scapular matrix, stained with toluidine blue and visualized by bright field; (D) a similar preparation observed using VPDFC. Note the absence of any birefringence in the empty vascular canals, independently on matrix preparation. Optical magnification and/or sizes of all makers are depicted in the images. Each image represents the result of a sample selected from an average of three different experiments.

of the molecular *milieu* chosen for coating PLLA. Finally, the 3D microarchitecture of the collagen coating and its capacity to act as a substrate for adhesion and growth of MSC-like cells were established at the ultrastructural level, and with computational morphometry. As shown in Figure 15, SEM analysis of collagen-coated PLLA revealed a mesh of thin fibers variably interconnected, giving rise to a repeatable microporous lattice whose pore sizes ranged from 875.86 ± 420.01 to 1024.50 ± 487.95 μnm^2, without any statistically significant difference between four different collagen replicates ($p = .7$). Once seeded on this biomaterial, MSC-like cells (mouse embryonic Swiss 3 T3 fibroblasts) strongly adhered to it, and exhibited a sustained growth. We concluded that the PLLA-rat tail collagen biomaterial could be used in vitro as a simplified microanatomical surrogate of the perivascular ECM around the wall of the cancellous vessels. (Data courtesy of Andrea Faccini, "Centro Misure Giuseppe Casnati" and Marco Alfieri, PhD Program in Molecular Medicine 2015–2018, UNIPR, Parma, Italy).

3.5 | Osteoporotic lesions in the human jaw and tarsus reveal cues for engineering a 3D human bone organoid

To get some cues whether the constructive principles of our compartment-related 3D rat organoid could represent a basis for eventual engineering of a human organoid suitable to in vitro investigate the behavior of human MSCs in osteoporotic flat and short bones, we in vivo searched for osteoporotic lesions in the human jaw and foot tarsus. As shown in Figure 16, in our human sample, jaw osteoporosis primarily affected the cortical compartment. In contrast, tarsal osteoporosis extensively involved the cancellous compartment. Thus, osteoporotic lesions were not randomly distributed but likely reflected mechanical, microstructural, and molecular peculiarities of the cortical with respect to cancellous compartments. Such an assumption was substantiated at a statistical level, as reported in Figure 17. Using clinical standards to classify a patient as osteoporotic (i.e. changes in bone mass density at the lumbar column and femur, surgical inspection during tooth implant), we observed that 14.3% of patients exhibited reabsorption of the cortical layer of the mandibular body, whereas 7.1% displayed frailty lesions of the tarsus (astragalus, calcaneus), affecting primarily most of the cancellous compartment and only a minimal fraction of cortical bone. Collectively, these data highlighted an anatomical specificity of the osteoporotic lesions in jaw and tarsal bone, that is, their preeminent location in one of the two bone compartments. This result suggested us that a suitable model of organoid for in vitro studying the behavior of human MSCs in flat and short bones under experimental osteoporotic conditions should retain the 3D microanatomy of cortical and cancellous compartments, as in the case of our 3D rat organoid. Thus, the principles we applied to engineer our 3D bone construct could profitably be used to engineer a similar human bone organoid.

4 | DISCUSSION

It is now increasingly recognized that functional efficiency of an in vitro/ex situ-engineered human and mammalian bioartificial organ relies on recapitulation of its three-dimensional (3D) micro- and macroarchitecture[34–36] including bones with their different cortical and cancellous compartments,[22] the latter hosting BM with most of bone immune cells.[3,37,38] Taking inspiration from the seminal work by Mina Bissel,[39] since 2007, our group has been studying this requirement for ex situ engineering of endocrine, parenchymal, and immunoregulatory organs.[23,27,32,40–49] We originally coined the term "organomorphism" to signify the need of a native organ morphology to reach adequate tissue function: It is based on topobiological/tensegrital inputs[50–52] provided by key mechano-chemical interactions between seeded cells and the surrounding stromal and vascular 3D structures[53] or stromal-vascular scaffold. Presence of an organ-specific stromal-vascular scaffold allows to establish cell–substrate connections ensuring specific anatomical distribution and functions to the growing cells.[27,28,40,45,54] As a result, cells may cope with the multiple physical constraints of their 3D microenvironment,[55] which we
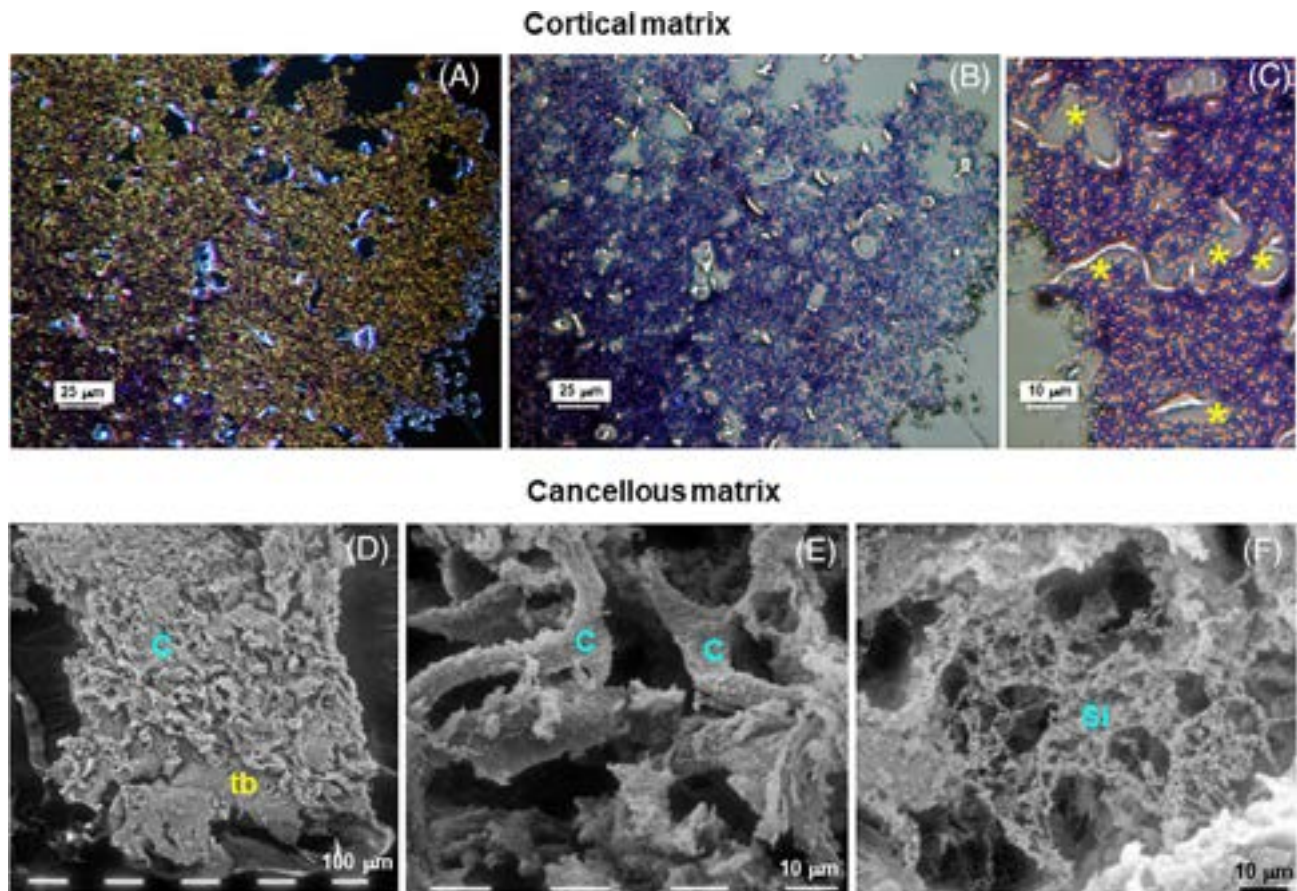
Cortical matrix

Cancellous matrix

FIGURE 12 VPDFC light microscopy and SEM, following reconstruction of intrinsic vessels with PLLA in the decellularized scapular matrix. (A) In the cortical compartment, VPDFC enlightened the striking birefringence (light blue) of the vascular walls lined by a layer of polymerized PLLA. This internal PLLA coating was confirmed (B,C) using single phase-contrast light microscopy, as white bands of biomaterial outlining the empty vascular canals (asterisks). In the cancellous compartment, SEM revealed (D,E) bunches of PLLA-reconstituted blood vessels/capillaries (c) in association with cancellous trabeculae (tb). In addition, (F) very fine PLLA-reconstituted sinusoids (Si) were observed in all cancellous spaces. Optical magnification and/or sizes of all makers are depicted in the images. Each image represents the result of a sample selected from an average of three different experiments.

suggested may act like a physical guide inside the 3D borders of their tissue/organ.[45,49] This behavior coincides with that stemming from the theory of Topobiology in tissue development/regeneration.[50,56] Experimentally, it relies on the possibility of offering to growing cells a 3D microenvironment with a composition and geometry corresponding to those naturally present during their either prenatal or postnatal/adult development, leading to variable differentiation trajectories.[27] Along with this line of evidence, reengineering developmental steps in an adult microenvironment was proposed as a successful basis for tissue regeneration.[57]

4.1 | Regulation of the bone cells in relation to the bone compartment

Quite distinct functional properties pertain to cancellous with respect to cortical bone compartments, In particular, in mouse long bones stroma and vessels of the cancellous compartment provide architectural and physiological specificity to resident MSCs,[20,21] influencing trabecular osteogenesis.[58] Similarly, selective cancellous bone loss by reduced osteogenic differentiation of MSCs occurs in the femur and tibia of high-fat-fed mice.[59] In contrast, in mouse vertebral bone anabolic effects of parathyroid hormone (PTH) involve two different molecular inputs: One acting in the cancellous compartment, through BM T lymphocytes triggering trabecular enlargement[60] as opposed to another restricted to osteoblasts and osteocytes of the cortical compartment, leading to thickened osteonic lamellae.[61] An astonishing example of site-related selectivity is offered by the mouse flat calvaria and short vertebral bones, where only the cancellous compartment hosts a special population of immunomodulatory monocytes and B lymphocytes migrating into the meninges and nervous tissue through endothelial cortical microchannels,[62] to elicit immune-mediated responses of the brain as those occurring in human neurodegenerative disorders.[63,64] Finally, in basal conditions, bone 3D microanatomy and related compartment geometry of blood vessels regulate the microtopography of bone immune cells.[13] Overall, cancellous bone has higher osteoinductive properties than cortical bone,[65] and during fracture healing, there is a different

FIGURE 13 Mass spectrometry (MS) analysis (LTQ-Orbitrap XL) of the collagen composition of adult male rat tail tendons. Note that the main collagen types are 1 and 3, as those present in the bone ECM. The graph represents the integration of two different and separate MS evaluations.

timescale in spatial location for osteogenetic and inflammatory cells in cancellous versus cortical layers.[66] Collectively, it emerges that cortical and cancellous bone compartments have different functional properties, the 3D architecture of their stromal-vascular scaffold contributes to the microtopographic constraints of resident bone cells, and these characteristics change in relation to the type of bone (either long, or short, or flat). Thus, it seemed to us desirable to have a flexible microenvironmental assay for the in vitro investigation of bone remodeling in specific bone compartments of flat and short bones.

4.2 | The 3D scapular matrix retains microanatomy consistent with flat and short bones

To engineer a bone experimental model whose 3D microanatomy is compatible with that of both flat and short bones including native tensegrital, mechano-chemical, and topobiological inputs, we chose the decellularized/decalcified 3D matrix of the adult male rat scapula. This bone is largely composed of a flat region (the scapular blade) consisting of two cortical layers and an intermediate cancellous space rich in trabeculae and BM. In addition, scapular vessels enter the cortical layers through their thicker parts, presumably making it easy to trace their path across the compact and spongy compartments. Only the thinnest cortical parts receive selective

vascularization from the periosteum.[67] To a reasonable extent, this anatomical arrangement recapitulates that of the jaw and tarsal bones, increasing the chance that 3D microtopography of eventually seeded osteoregulatory cells will become reproducible in most of the 3D scapular matrix.

Using a well-established methodology for bone decellularization[22] implemented with a preliminary 24-h freeze–thaw procedure,[23] we prepared decellularized and decellularized-decalcified 3D stromal matrices of the rat scapula. Satisfactory removal of contaminating DNA was obtained, without the need to perfuse the entire bone with buffer through vascular pedicles to remove cellular debris. With this technique, residual DNA levels were much lower than those commonly recommended (less than 50 ng DNA/mg dry weight) as an acceptable threshold for successful decellularization,[68] indicating adequacy of the protocol applied. Consistent with this evidence, light microscopic and ultrastructural studies confirmed removal of all cell types from bone connective layers (periosteum, endosteum) and compartments (cancellous and cortical) and, when we also removed the mineral mass, the native 3D organization of the scapular stromal-vascular scaffold remained morphologically unaltered, including its empty vascular conduits. In particular, a "ghost" matrix of the entire 3D scapula was obtained, having a macro- and microscopic morphology identical to that of the control bone, whereas trabecular and cortical layers resulted deprived of osteoblasts, osteoclasts, lacunar osteocytes, and any signs of calcified tissue. Remarkably, the

demineralized fibrous matrix emerged as a compact and regular structure made of collagen bundles replicating the 3D morphology of cancellous trabeculae, cortical lamellae, and osteocyte lacunae similar to control and decellularized bones. Collectively, a very satisfactory maintenance of bone type-dependent microanatomy was achieved.

4.3 | Cell compatibility of the 3D scapular organoid

As a proof-of-concept of cell compatibility and compartment-related properties of this 3D bone construct, we tested it suitability to in vitro host and support growth of a well-established type of bone osteogenic cells, adult male rat BM-derived MSCs (rBMSCs). This is a well-known strategy, traditionally applied to natural bone matrices when using bone-forming cells.[1-3] Following organoid recellularization, a difference in the timescale of osteogenetic commitment emerged between MSCs colonizing cancellous versus cortical layers, independently on a previous short-term "boost" by a rotation-tilt apparatus expected to favor attachment to the 3D matrix. In particular, only MSCs reaching the spongy trabeculae exhibited signs of skeletogenic determination (aggregation in insulae, secretion of de novo synthesized ECM) as opposed to simple cell accumulation in the cortical
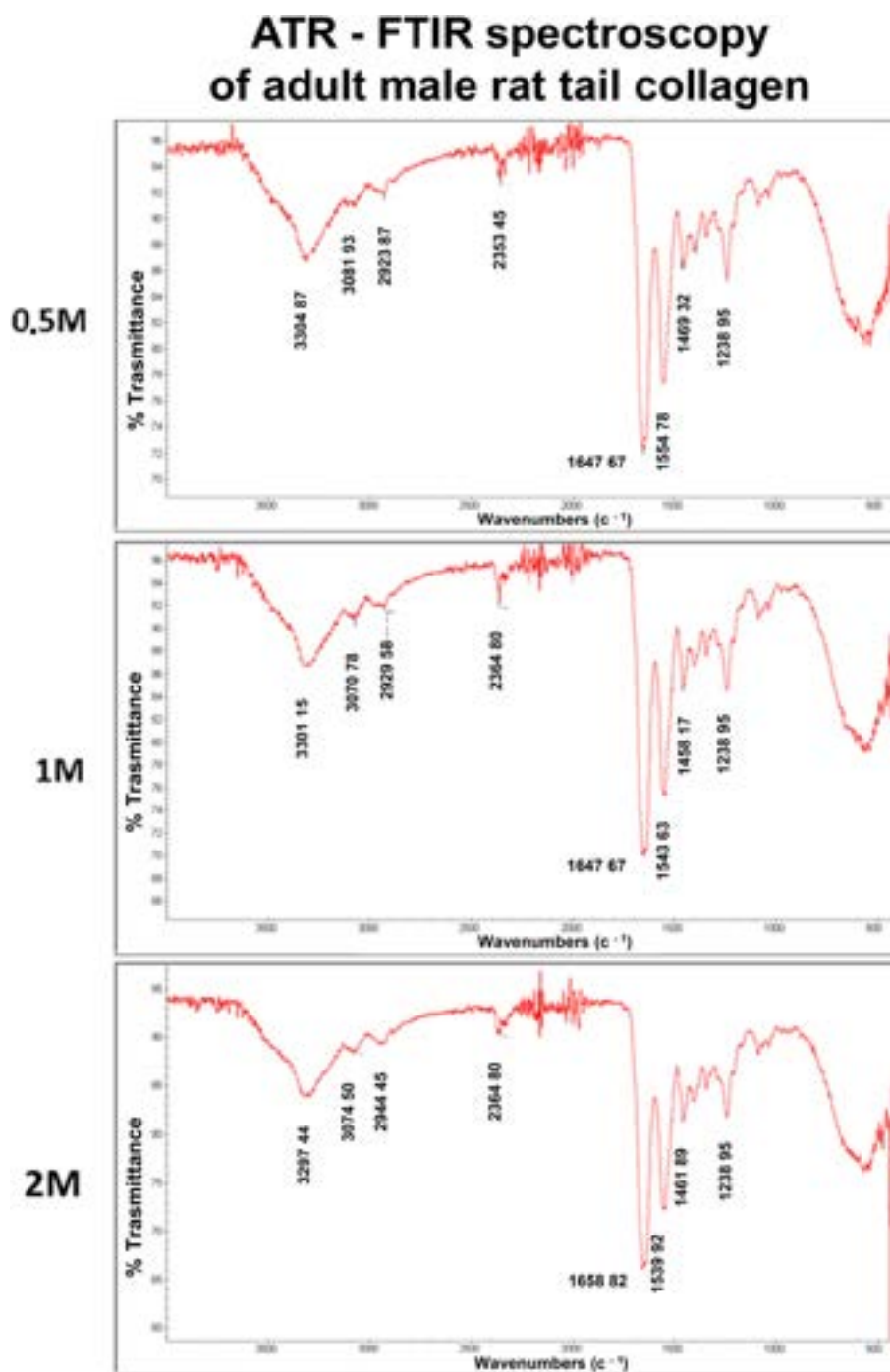
FIGURE 14 Spectra of rat tail collagen solution obtained by ATR-FTIR spectroscopy. Morphology and wavelengths of the spectroscopic peaks indicated that number and type of chemical bonds did not change at increasing concentrations (0.5–2 M) of the solubilizing agent (acetic acid), suggesting structural stability of the collagen mixture. Each spectrum is representative of a sample chosen between three different experiments.

lamellae without morphological evidence of programming toward a mineralization process. This difference was maintained up to 6 weeks of matrix colonization, and was reverted by the use of a differentiation medium leading to an osteogenic lineage in both compartments, including release of matrix vesicles and mineral mass deposition. Overall, the cancellous compartment was found to promoted a sort of "MSC skeletal specification" conditioned by its fibrous environment (keeping the trabecular endosteum), whose the cortical one (retaining both endosteum and periosteum) seemed to be missing. Supposedly differences in substrate elasticity, geometry, mechanical forces, and ECM molecules brought into play by cancellous with respect to

cortical fibrous matrices and linings might have played a relevant commitment role.[69] Support to this hypothesis is provided by the evidence that MSCs of the cancellous metaphysis of the mouse femur exhibit different molecular properties than MSCs of the cortical endosteum of the diaphysis.[70]

4.4 | Reconstruction of matrix vessels with PLLA

To increase the microanatomical similarity between the engineered organoid and a native stromal-vascular matrix of a flat and short bone,
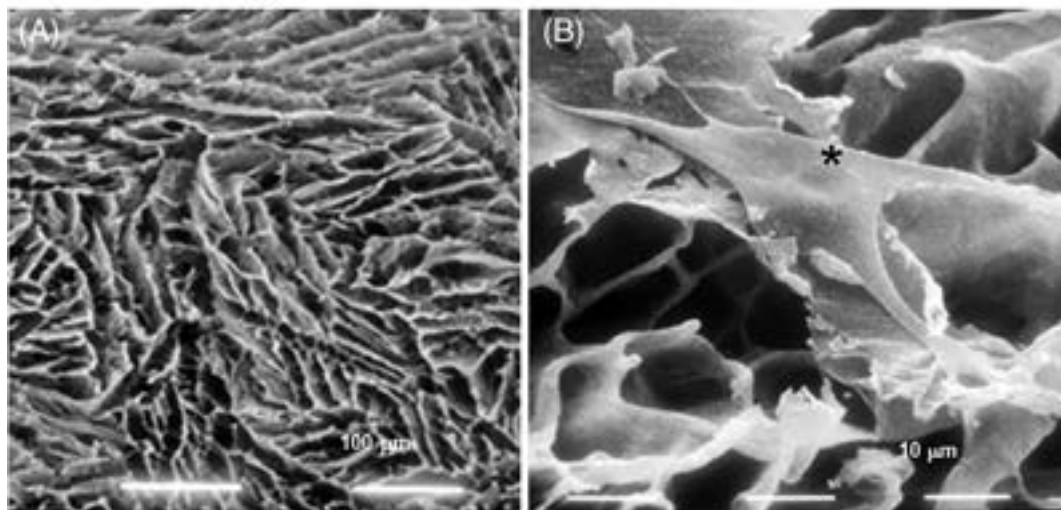
FIGURE 15 (A) SEM image of criodehydrated 2% (w/v) rat tail collagen, coating polymerized PLLA. The coating was organized into fibers of different lengths, giving rise to interconnected spaces (micropores) suitable for adhesion of eventually seeded cells. The image represents the result of a sample selected from four different experiments; (B) Swiss NIH 3T3 mouse embryonic fibroblast (asterisk) attached to lyophilized rat tail collagen, coating polymerized PLLA. This evidence confirmed adequacy of the PLLA-rat tail collagen biomaterial to favor perivascular growth and attachment of MSC-like cells. Sizes of all makers are on the image; it depicts the result of a sample selected from four different experiments.
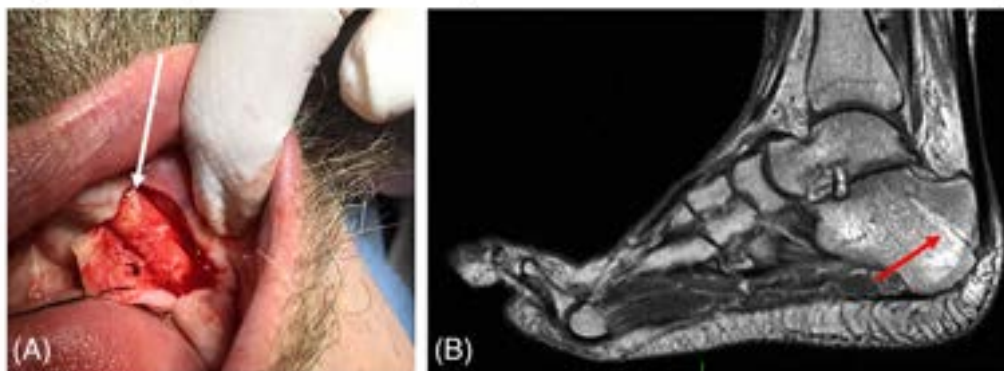

FIGURE 16 (A) Edentulous male patient (age 59 years) showing severe atrophy and reabsorption of the mandibular bone. Surgical displacement of the gum and periosteum for dental implants revealed porosity in the upper part of the exposed bone, where the compact cortical layer was eroded (arrow); (B) MRI image of a nonunion foot fracture from a female postmenopausal patient (age 76 years), exhibiting bone frailty largely in cancellous (arrow) and only partially cortical compartments of the calcaneus.

we reconstructed the walls of the intrinsic bone vessels directly inside the cortical and cancellous compartments. Indeed, recent data highlight the coupling of angiogenesis with osteogenesis by osteoprogenitors through activation of specific molecular pathways by bone capillaries subtypes.[58] It is not yet known whether this vascular osteoinduction is exquisitely related to intercellular paracrine interaction or may also rely on topobiological mechanochemical interactions brought about by the perivascular ECM and the geometry of blood vessels and sinuses per se. In parenchymal organs like the thyroid gland, anterior pituitary, and thymus, we have collected evidence that vascular geometry per se may play a specific role in addressing the fate of surrounding cells.[27,28,40,41,45,47,49] In our 3D bone organoid model, reconstruction of intrinsic blood vessels conforms to the concept of organomorphism that targets the role of the 3D vascular geometry per se in favoring bone cell commitment.

As we have previously tested in a number of organ's model,[25,26,71–74] we perfused the scapular vascular pedicles with a solution of thermoplastic material, the biocompatible polylevolactic acid (PLLA).[28] Then, based on an hoc developed modification of a phase dark-field contrast light microscopic technique,[30] we observed a striking birefringence of the polymerized PLLA lining blood vessel walls in the decellularized cortical compartment, as expected for the crystalline structure of this polymer.[75] Detailed analysis of the cancellous compartment by SEM revealed PLLA-dependent reconstitution

Clinical data related to the presence of osteoporosis in our human sample

Patient	Age	Vertebral T score	Femur T score	Jaw cortical lesions	Tarsus cancellous lesions
female	76	− 2.3	− 2.0	n.d.	++
female	40	normal	normal	n.d.	n.d.
female	21	normal	normal	n.d.	n.d.
female	57	normal	normal	n.d.	n.d.
male	55	normal	normal	n.d.	n.d.
female	53	normal	normal	n.d.	n.d.
female	54	− 4.2	?	?	?
female	81	− 1.9	− 1.6	n.d.	n.d.
male	58	normal	normal	+	n.d.
female	59	normal	− 2.3	n.d.	n.d.
female	53	normal	normal	n.d.	n.d.
male	28	normal	normal	n.d.	n.d.
female	56	− 3.3	− 3.2	n.d.	n.d.
female	59	nomal	normal	n.d.	n.d.
male	44	normal	normal	n.d.	n.d.
female	43	normal	normal	n.d.	n.d.
male	57	normal	normal	n.d.	n.d.
female	21	normal	normal	n.d.	n.d.
female	59	normal	normal	n.d.	n.d.
female	59	normal	− 1.1	n.d.	n.d.
female	76	− 2.3	− 2.0	n.d.	++
male	59	?	?	++	n.d.
male	74	?	?	++	n.d.
female	74	?	?	++	n.d.
female	58	− 3.3	− 3.1	n.d.	n.d.
female	49	normal	normal	n.d.	n.d.
female	50	normal	normal	n.d.	n.d.
female	32	normal	normal	n.d.	n.d.

FIGURE 17 Distribution of normal versus osteopenic/osteoporotic patients, as retrospectively determined either by analysis of densitometric T score at the lumbar column and/or femur or direct surgical inspection, as in the case of jaw lesions. + = initial erosion; ++ = advanced erosion; n.d. = not determined; ? = not known (evaluation by two different clinical observers).

of tufts of blood vessels and fine capillaries/sinusoids filling the empty intertrabecular spaces originally occupied by BM, confirming suitability of this biomaterial to reproduce the fine anatomy of intrinsic bone vascular canals, as we have already observed in other organs.[28] The choice of this bioerodible biomaterial was motivated by our previous evidence that PLLA may ensure survival, replication, microvesicular release, and immunophenotype stability of rBMSCs.[32]

Finally, to increase the biomimesis of the PLLA-fabricated vascular walls, we exploited the knowledge that collagen types 1 and 3 provide perivascular support to MSCs, immune, and osteoprogenitor cells in the BM, and are involved in cortical and trabecular osteogenesis.[76,77] Indeed, we had previously shown that collagen fibers may trigger biomimetic mineralization by inducing nucleation of hydroxyapatite, leading to osteogenic differentiation and mineral deposition.[32,78] Thus, we coated PLLA-reconstructed vascular channels with rat tail collagen, found rich in bone-specific collagens by mass spectrometric analysis, and capable of forming a lattice-like geometry on the surface of the polymerized PLLA. Indeed, previous studies showed suitability of rat tail collagen for vascular network self-assembly in microphysiological systems[79] based on its capacity to undergo fibrillogenesis in a cell culture pH and temperature environment.[80] As a result, we observed attachment and survival of seeded mouse embryonic fibroblasts, chosen as an experimental surrogate of rat osteogenetic MSCs.[81] We concluded that our biocompatible PLLA-collagen composite could in vitro mimic the "vasculature - perivascular stroma" complex of rat bones, raising the possibility that it may favor MSCs function as in vivo occurring in bone niches.[14–17]

4.5 | In vivo site-specific osteoporosis suggests site-specific organoids for its in vitro study

An in vivo clinical condition of human osteoporotic lesions selectively involving either the cortical or cancellous compartments is offered by two flat and short bones, the jaw and tarsus of the foot. Indeed, recent studies have highlighted that reduction in bone density, and alterations in the 3D organization and quality of the bone tissue may early involve the cortical lamellae of the jaw as opposed to the tarsal cancellous trabeculae.[82,83] Using an unselected sample of outpatient subjects with a wide age range and evidence of normal weight/ overweight /obesity, we initially sought reduction in bone mass density (BMD) as it is known to occur in primary osteoporosis.[84,85] Osteopenic/osteoporotic BMD was retrospectively acquired at classical bone sites (lumbar vertebral column, femoral head), and found in 28.6% of the subjects, a percentage consistent with current epidemiological data.[86] Supported by the clinical representativeness of our sample, we searched for lesions affecting the jaw and foot tarsus in the absence of local secondary osteoporosis from chronic periodontal disease, drug toxicity, and excess mechanical stress.[87–89] We found evidence of mandibular cortical resorption, corresponding to destruction of compact lamellae,[90] and mainly cancellous (and only minimally cortical) tarsal frailty up to nonunion fracture, corresponding to disorganized and weakened cancellous trabeculae,[90] in a percentage

comparable to that observed in previous studies.[82,89] These data confirmed that in humans, the primary osteoporotic process of jaw and tarsus differently affected cortical versus cancellous compartments, depending on the type of bone (i.e. jaw and tarsus respond with different, site-specific lesions).

Indeed, nonunion fractures such as those observed in our tarsal cases recognize precocious senescence and reduced capacity of cancellous MSCs to elicit an osteoblastic response,[91] and its well established that osteoporosis may develop in different sites (cancellous or cortical) of the same bone but with different rates and extensions or may cause selective damage to cortical or cancellous sites depending on the type of bone.[90] Therefore, the methodology used to engineer our rat 3D prototype might be exploited to obtain an equivalent human 3D bone organoid, useful for studying in vitro the functional derangement of human MSC in relation to the bone compartment, under experimental osteoporotic challenge. In particular, it would be possible to decide which, when, and how many osteogenic or immunomodulatory/immune cells add to the bone system to increase the complexity of the cellular interplay. In this manner, the relative contributions of different cell types to the osteoporotic bone lesions in specific bone compartments (cancellous and/or cortical) could be enlightened. A similar conceptual design has recently been proposed to in vitro dissect the osteoimmunomodulation process in dependence on different substrate biomaterials.[92]

Overall, a similar type of 3D bone organoid might take advantage of at least three technical aspects. Since we and others have shown that the decellularization process, sex and age of the donors may modify availability of matrix components in both visceral organs like the thyroid, liver, pancreas, kidney, and skin of rats and pigs,[23,48] and in young versus aged human bones,[93] constancy in the choice of these methodological variables should ensure constancy of remodeling response to the tested bone cell array. In addition, the PLLA-reconstructed vascular channels might represent an excellent source for in vitro bioengineering of the delivery of osteomodulatory substances like vitamin D,[94] biomimetic hydroxyapatites,[78] and growth factors/transcripts like PDGFalfa, PDGFbeta TGFbeta1, TGFbeta3, FGF1, and HIF-1alfa involved in osteogenetic angiogenesis.[58] Finally, substitution of PLLA with rapidly bioerodible substrates such as reticulated collagen is expected to lead to a fenestrated-like structure of the reconstituted vascular walls,[28] suitable for transmural recirculation of seeded cells between the vascular/capillary lumen and the bone compartments,[95] typically deranged in osteoporosis[96,97] as well as provide osteoconductive pathways for anatomical regeneration of vascular walls by endothelial cells, as expected in cases of biomimetic material implants.[98]

5 | CONCLUSIONS

The bioartificial organoid model and related component biomaterials presented here are inspired to a strong biomimesis with the original 3D microanatomy of mammalian flat and short bones. The purpose was to provide a bone type-specific, compartment-based microenvironment allowing for a space-dependent evaluation of bone remodeling, possibly

applicable for studying the selectivity of bone lesions in human disorders like osteoporosis. In a broader perspective, we believe the proposed organoid may help to understand a number of bone microtopographic mechanisms, thus triggering the design/discovery of novel compartment-related molecules to enhance a personalized therapy of osteoporosis based on a "locality cross - talk" of different bone cell types.

CONFLICT OF INTEREST STATEMENT

All the authors have no conflicts of interest relevant to this article.

DATA AVAILABILITY STATEMENT

The data that support the findings of this study are available from the corresponding author upon reasonable request.

ORCID

Roberto Toni https://orcid.org/0000-0002-5081-4753

REFERENCES

1. Chen G, Lv Y. Decellularized bone matrix scaffold for bone regeneration. *Methods Mol Biol*. 2018;1577:239-254.
2. Mattioli-Belmonte M, Montemurro F, Licini C, et al. Cell-free demineralized bone matrix for mesenchymal stem cells survival and colonization materials. *Materials (Basel)*. 2019;12:1360.
3. Bourgine PE, Martin I, Schroeder T. Engineering human bone marrow proxies. *Cell Stem Cell*. 2018;22:298-301.
4. Krupnick AS, Shaaban A, Radu A, Flake AW. Bone marrow tissue engineering. *Tissue Eng*. 2002;8:145-155.
5. Di Buduo CA, Soprano PM, Tozzi L, et al. Modular flow chamber for engineering bone marrow architecture and function. *Biomaterials*. 2017;14:60-71.
6. Braham MVJ, Ahlfel T, Akkineni AR, et al. Endosteal and perivascular subniches in a 3D bone marrow model for multiple myeloma. *Tissue Eng Part C*. 2008;24:300-312.
7. Akiva A, Melke J, Ansari S, et al. An organoid for woven bone. *Adv Funct Mater*. 2021;31:2010524.
8. Iordachescu A, Amin HD, Rankin SM, et al. An in vitro model for the development of mature bone containing an osteocyte network. *Adv Biosyst*. 2017;2:1700156.
9. Iordachescu A, Hulley P, Grover LM. A novel method for the collection of nanoscopic vesicles from an organotypic culture model. *RSC Adv*. 2018;8:7622-7632.
10. Iordachescu A, Williams RL, Hulley P, Grover LM. Organotypic culture of bone-like structures using composite ceramic-fibrin scaffolds. *Curr Protoc Stem Cell Biol*. 2019;48:e79.
11. Park Y, Cheong E, Kwak J-G, Carpenter R, Shim J-H, Lee J. Trabecular bone organoid model for studying the regulation of localized bone remodeling. *Sci Adv*. 2021;7:eabd6495.
12. Iordachescu A, Hughes EAB, Joseph S, et al. Trabecular bone organoids: a micron-scale 'humanised' prototype designed to study the effects of microgravity and degeneration. *NPJ Microgravity*. 2021;7:17.
13. Toni R, Di Conza G, Barbaro F, et al. Microtopography of immune cells in osteoporosis and bone lesions by endocrine disruptors. *Frontiers Immunol*. 2020;11:1737.
14. Nagasawa T, Omatsu Y, Sugiyama T. Control of hematopoietic stem cells by the bone marrow stromal niche: the role of reticular cells. *Trends Immunol*. 2011;32:315-320.
15. Bianco P, Sacchetti B, Riminucci M. Osteoprogenitors and the hematopoietic microenvironment. *Best Pract Res Clin Haematol*. 2011;24: 37-47.
16. Sugiyama T, Nagasawa T. Bone marrow niches for hematopoietic stem cells and immune cells. *Inflamm Allergy Drug Targets*. 2012;11:201-206.
17. Cordeiro-Spinetti E, Taichman RS, Balduino A. The bone marrow endosteal niche: how far from the surface? *J Cell Biochem*. 2015;116: 6-11.
18. Cowin CS, Cardoso L. Blood and interstitial flow in the hierarchical pore space architecture of bone tissue. *J Biomech*. 2015;48:842-854.
19. Grüneboom A, Hawwari I, Weidner D, et al. A network of transcortical capillaries as mainstay for blood circulation in long bones. *Nat Metab*. 2019;1:236-250.
20. Nombela-Arietta C, Manz MG. Quantification and three-dimensional microanatomical organization of the bone marrow. *Blood Adv*. 2017; 1:407-416.
21. Gomariz A, Helbling PM, Isringhausen S, et al. Quantitative spatial analysis of haematopoiesis-regulating stromal cells in the bone marrow microenvironment by 3D microscopy. *Nat Commun*. 2018;9:2532.
22. Grayson WL, Fröhlich M, Yeager K, et al. Engineering anatomically shaped human bone grafts. *Proc Natl Acad Sci USA*. 2010;107:3299-3304.

23. Alfieri M, Barbaro F, Consolini E, et al. A targeted mass spectrometry method to screen collagen types I-V in the decellularized 3D extracellular matrix of the adult male rat thyroid. *Talanta*. 2019;193:1-8.

24. Toni R, Jackson IMD, Lechan RM. Neuropeptide-Y-immunoreacive innervation of thyrotropin-releasing hormone-synthesizing neurons in the rat hypothalamic paraventricular nucleus. *Endocrinology*. 1990;26:2444-2453.

25. Toni R, Favero L, Bolzani R. Further observations on the anatomical variation in the arteries of the human pancreas. *IRCS Med Sci*. 1985;13:605-606.

26. Toni R, Mosca S, Favero L, et al. Clinical anatomy of the suprarenal arteries: a quantitative approach by aortography. *Surg Radiol Anat*. 1988;10:297-302.

27. Toni R, Tampieri A, Zini N, et al. Ex situ bioengineering of bioartificial endocrine glands: a new frontier in regenerative medicine of soft tissue organs. *Ann Anat*. 2011;193:381-394.

28. Sprio S, Sandri M, Iafisco M, et al. Biomimetic biomaterials in regenerative medicine. In: Ruys AJ, ed. *Biomimetic Biomaterials, Structure and Applications*. Whoodhead Publishing; 2013:3-45.

29. Muschler GF, Raut VP, Patterson TE, Wenke JC, Hollinger JO. The design and use of animal models for translational research in bone tissue engineering and regenerative medicine. *Tissue Eng Part B*. 2010;16:123-145.

30. Piper T, Piper J. Variable phase dark-field contrast: a variant illumination technique for improved visualizations of transparent specimens. *Microsc Microanal*. 2012;18:343-352.

31. Chambard M, Gabrion J, Mauchamp J. Influence of collagen gel on the orientation of epithelial cell polarity: follicle formation from isolated thyroid cells and from preformed monolayers. *J Cell Biol*. 1981;91:157-166.

32. Zamparelli A, Zini N, Cattini L, et al. Growth on poly(L-lactic acid) porous scaffold preserves CD73 and CD90 immunophenotype markers of rat bone marrow mesenchymal stromal cells. *J Mater Sci Mater Med*. 2014;25:2421-2436.

33. Harting M, Jimenez F, Pati S, Baumgartner J, Cox C Jr. Immunophenotype characterization of rat mesenchymal stromal cells. *Cytotherapy*. 2008;10:243-253.

34. Koh C, Atala A. Tissue engineering, stem cells, and cloning: opportunities for rigenerative medicine. *J Am Soc Nephrol*. 2004;15:1113-1125.

35. Furth ME, Atala A. Producing organs in the laboratory. *Curr Urol Rep*. 2008;9:433-436.

36. Atala A. Engineering organs. *Curr Opin Biotechnol*. 2009;20:575-592.

37. Bourgine PE, Klein T, Paczullac AM, et al. In vitro biomimetic engineering of a human hematopoietic niche with functional properties. *Proc Natl Acad Sci USA*. 2018;115:E5688-E5695.

38. Bianco JER, Rosa RG, Congrains-Castillo A, et al. Characterization of a novel decellularized bone marrow scaffold as an inductive environment for hematopoietic stem cells. *Biomater Sci*. 2019;7:1516-1528.

39. Bissel MJ. Architecture is the message: the role of extracellular matrix and 3-D structure in tissue-specific gene expression and breast cancer. *Pezcoller Found J*. 2007;16(29):2-17.

40. Toni R, Della Casa C, Spaletta G, et al. The bioartificial thyroid: a biotechnological perspective in endocrine organ engineering for transplantation replacement. *Acta Biomed*. 2007;78(Supp 1):129-155.

41. Toni R, Della Casa C, Bodria M, et al. A study on the relationship between intraglandular arterial distribution and thyroid lobe shape: implications for biotechnology of a bioartificial thyroid. *Anat Ann*. 2008;190:432-441.

42. Strusi V, Zini N, Dallatana D, et al. Ex situ bioengineering of the rat thyroid using as a scaffold the three dimensional (3D) decellularized matrix of the glandular lobe: clues to the organomorphic principle. In: abstracts 65th congress of SIAI, Padua, Italy, September 27–29, 2011. *It J Anat Embryol*. 2011;116(Suppl 1):S180.

43. Strusi V, Zini N, Dallatana D, et al. Endocrine bioengineering: reconstruction of a bioartificial thyroid lobe using its three-dimensional (3D) stromal/vascular matrix as a scaffold. In: Abstracts ICE/ECE Congress, Florence, Italy, May 5–9, 2012. *Endocr Abstracts*. 2012;29:P1586.

44. Toni R, Strusi V, Zini N, et al. Bioengineering of the thyroid lobe: use of its stromal/vascular matrix as a scaffold for ex situ reconstruction. In: abstracts 94th meeting of the Endocrine Society, Huston, TX, USA, June 23–26, 2012. *Endocr Rev*. 2012;33: (03_Meeting Abst): OR26-3.

45. Toni R, Bassi E, Zini N, et al. Bioartificial endocrine glands: at the cutting edge of translational research in endocrinology. In: Sprio S, Tampieri A, eds. *Bio-Inspired Regenerative Medicine: Material, Processes, and Clinical Applications*. Pan Standford Publishing; 2016:357-387.

46. Moroni L, Barbaro F, Caiment F, et al. SCREENED: a multistage model of thyroid gland function for screening endocrine-disrupting chemicals in a biologically sex-specific manner. *Int J Mol Sci*. 2020;21:3648.

47. Asnaghi MA, Barthlott T, Gullotta F, et al. Thymus extracellular matrix-derived scaffolds support graft-resident thymopoiesis and long-term in vitro culture of adult thymic epithelial cells. *Adv Funct Mater*. 2021;31:2010747.

48. Remaggi G, Barbaro F, Di Conza G, et al. Decellularization detergents as methodological variables in mass spectrometry of stromal matrixes. *Tissue Eng Part C*. 2022;28:148-157.

49. Spaletta G, Sofroniou M, Barbaro F, Di Conza G, Mosca S, Toni R. A computational template for 3D modelling of the vascular scaffold of the human thyroid gland. *Tissue Eng Part A*. 2023;29(1–2):47-57.

50. Edelman GM. *Topobiology, An Introduction to Molecular Embryology*. Basic Book Inc; 1988.

51. Ingber DE. Cellular tensegrity: defining new rules of biological design that govern the cytoskeleton. *J Cell Sci*. 1993;104:613-627.

52. Ingber DE. Mechanical control of tissue growth: function follows form. *Proc Natl Acad Sci USA*. 2005;102:11571-11572.

53. Chuong CM, Wu P, Plikus M, Jiang TX, Widelitz RB. Engineering stem cells into organs: topobiological transformations demonstrated by beak, feather, and other ectodermal organ morphogenesis. *Curr Top Dev Biol*. 2006;72:237-274.

54. Engler AJ, Humbert PO, Wehrle-Haller B, Weaver VM. Multiscale modeling of form and function. *Science*. 2009;324:208-212.

55. Streichana SJ, Hoernerb CR, Schneidtb T, Holzerb D, Hufnagelb L. Spatial constraints control cell proliferation in tissues. *Proc Natl Acad Sci USA*. 2014;111:5586-5591.

56. Toni R. Topobiology: epistemological implications of an ontic theory in biomorphology. *It J Philos Sci Epistemologia*. 2004;27:83-106.

57. Tonnarelli B, Centola M, Barbero A, Zeller R, Martin I. Re-engineering development to instruct tissue regeneration. *Curr Top Dev Biol*. 2014;108:319-338.

58. Kusumbe AP, Ramasamy SK, Adams RH. Coupling of angiogenesis and osteogenesis by a specific vessel subtype in bone. *Nature*. 2014;507:323-328.

59. Gautam J, Choudhary D, Khedgikar V, et al. Micro-architectural changes in cancellous bone differ in female and male C57BL/6 mice with high-fat diet-induced low bone mineral density. *Brit J Nutrit*. 2014;111:1811-1821.

60. Terauchi M, Li J-Y, Bedi B, et al. T lymphocytes amplify the anabolic activity of parathyroid hormone through wnt10b signaling. *Cell Metab*. 2009;10:229-240.

61. Li J-Y, Walke LD, Tyag AM, Adams J, Weitzmann MN, Pacifici R. The sclerostin-independent bone anabolic activity of intermittent PTH treatment is mediated by T-cell–produced wnt10b. *J Bone Min Res*. 2014;29:43-54.

62. Herisson F, Frodermann V, Courties G, et al. Direct vascular channels connect skull bone marrow and the brain surface enabling myeloid cell migration. *Nat Neurosci*. 2018;21:1209-1217.

63. Cugurra A, Mamuladze T, Rustenhoven J, et al. Skull and vertebral bone marrow are myeloid cell reservoirs for the meninges and CNS parenchyma. *Science*. 2021;373(6553):eabf7844.

64. Brioschi S, Wang W-L, Peng V, et al. Heterogeneity of meningeal B cells reveals a lymphopoietic niche at the CNS borders. *Science*. 2021; 373(6553):eabf9277.

65. Herford AS, Stoffella E, Stanford CM. Bone grafts and bone substitute materials. In: Torabinejad M, Sabeti MA, Goodacre CJ, eds. *Principles and Practice of Single Implant and Restorations*. Elsevier Saunders; 2014:75-86.

66. Bernhardsson M, Aspenberg P. Osteoblast precursors and inflammatory cells arrive simultaneously to sites of a trabecular-bone injury. *Acta Orthopaed*. 2018;89:457-461.

67. Pannarale L, Morini S, D'Ubaldo E, Gaudio E, Marinozzi G. SEM corrosion-casts study of the microcirculation of the flat bones in the rat. *Anat Rec*. 1997;247:462-471.

68. Crapo PM, Gilbert TW, Badylak SF. An overview of tissue and whole organ decellularization processes. *Biomaterials*. 2012;32:3233-3243.

69. Chen Q, Shou P, Zheng C, et al. Fate decision of mesenchymal stem cells: adipocytes or osteoblasts? *Cell Death Differ*. 2016;23:1128-1139.

70. Sivaraj KK, Jeong H-W, Dharmalingam B, et al. Regional specialization and fate specification of bone stromal cells in skeletal development. *Cell Rep*. 2021;36:109352.

71. Bassoli E, Denti L, Gatto A, et al. New approaches to prototype 3D vascular-like structures by additive layer manufacturing. In: Bártolo PJ, ed. *Innovative Developments in Virtual and Physical Prototyping*. CRC Press, Taylor & Francis; 2011:35-42.

72. Bassoli E, Denti L, Gatto A, et al. A combined additive layer manufacturing / indirect replication method to prototype 3D vascular-like structures of soft tissue and endocrine organs. *Virtual Phys Prototyp*. 2012;7:3-11.

73. Bassoli E, Denti L, Gatto A, et al. A planar fractal analysis of the arterial tree of the human thyroid gland: implications for additive manufacturing of 3D ramified scaffolds. In: Bártolo PJ, de Lemos ACS, Pereira AMH, et al., eds. *High Value Manufacturing: Advanced Research in Virtual and Rapid Prototyping*. CRC Press, Taylor & Francis; 2014: 423-429.

74. Bassoli E, Denti L, Gatto A, et al. Towards additive manufacturing of ramified scaffolds of the thyroid vascular system: a preliminary fractal analysis. *IJMET*. 2018;9:429-437.

75. Andreopulos AG, Hatzi E, Doxastakis M. Synthesis and properties of poly (lactic acid). *J Mater Sci Mater Med*. 1999;10:29-33.

76. Tzaphildou M. Bone architecture: collagen structure and calcium/phosphorus maps. *J Biol Phys*. 2008;34:39-49.

77. Volk SW, Shah SR, Cohen AJ, et al. Type III collagen regulates osteoblastogenesis and the quantity of trabecular bone. *Calcif Tissue Int*. 2014;94:621-631.

78. Tampieri A, Sprio S, Sandri M, Valentini F. Mimicking natural biomineralization processes: a new tool for osteochondral scaffold development. *Trends Biotechnol*. 2011;29:526-535.

79. Whelan IT, Moeendarbary E, Hoey DA, Kelly J. Biofabrication of vasculature in microphysiological models of bone. *Biofabrication*. 2021; 13:032004.

80. Achilli M, Mantovani D. Tailoring mechanical properties of collagen-based scaffolds for vascular tissue engineering: the effects of pH, temperature and ionic strength on gelation. *Polymers*. 2010;2: 664-680.

81. Dastagir K, Reimers K, Lazaridis A, et al. Murine embryonic fibroblast cell lines differentiate into three mesenchymal lineages to different extents: new models to investigate differentiation processes. *Cell Reprogram*. 2014;16:241-252.

82. Gulsahi A. Osteoporosis and jawbones in women. *J Int Soc Prev Community Dent*. 2015;5:263-267.

83. Kaiser PB, Guss D, Di Giovanni CW. Stress fractures of the foot and ankle in athletes. *Foot Ankle Orthop*. 2018;3(3):1-11.

84. Pagliari D, Tamburrelli FC, Zirio G, Newton EE, Cianci R. The role of bone immunological niche for a new pathogenetic paradigm of osteoporosis. *Anal Cell Pathol*. 2015;2015:434389.

85. Pietschmann P, Mechtcheriakova D, Meshcheryakova A, Föger-Samwald U, Ellinger I. Immunology of osteoporosis: a mini-review. *Gerontology*. 2016;62:128-137.

86. International osteoporosis foundation. https://www.osteoporosis.foundation/facts-statistics/epidemiology-of-osteoporosis-and-fragility-fractures (2021).

87. Giro G, Chambrone L, Goldstein A, et al. Impact of osteoporosis in dental implants: a systematic review. *World J Orthop*. 2015;6: 311-315.

88. Fassio A, Bertoldo F, Idolazzi L, Viapiana O, Rossini M, Gatti D. Drug-induced osteonecrosis of the jaw: the state of the art. *Reumatismo*. 2017;69:9-15.

89. Mills LA, Aitke SA, Simpson HRW. The risk of non-union per fracture: current myths and revised figures from a population of over 4 million adults. *Acta Othopaed*. 2017;88:434-439.

90. Brandi ML. Microarchitecture, the key to bone quality. *Rheumatology*. 2009;48:3-8.

91. Bajada S, Marshall MJ, Wright KT, Richardson JB, Johnson WE. Decreased osteogenesis, increased cell senescence and elevated Dickkopf-1 secretion in human fracture non union stromal cells. *Bone*. 2009;45:726-735.

92. Chen Z, Klein T, Murray RZ, Crawford R, Chang J, Wu C. Osteoimmunomodulation for the development of advanced bone biomaterials. *Mater Today*. 2016;19:304-321.

93. Smith CA, Board TN, Rooney P, Eagle MJ, Richardson SM, Hoyland JA. Human decellularized bone scaffolds from aged donors show improved osteoinductive capacity compared to young donor bone. *PLoS One*. 2017;12:0177416.

94. Papadimitropoulos A, Scherberich A, Güven S, Theilgaard N, Crooijmans HJA, et al. A 3D in vitro bone organoid model using human progenitor cells. *Europ Cell Mater*. 2011;21:445-458.

95. Bianco P, Cao X, Frenette PS, et al. The meaning, the sense and the significance: translating the science of mesenchymal stem cells into medicine. *Nat Med*. 2013;19:35-42.

96. Osterhoff G, Morgan EF, Shefelbine SJ, Karim L, McNamara LM, Augat P. Bone mechanical properties and changes with osteoporosis. *Injury*. 2016;47:11-20.

97. Bernhard A, Milovanovic P, Zimmermann EA, et al. Micro-morphological properties of osteons reveal changes in cortical bone stability during aging, osteoporosis, and bisphosphonate treatment in women. *Osteoporosis Int*. 2013;24:2671-2680.

98. Tampieri A, Sprio S, Ruffini A, Celotti G, Lescib G, Roveri N. From wood to bone: multi-step process to convert wood hierarchical structures into biomimetic hydroxyapatite scaffolds for bone tissue engineering. *J Mater Chem*. 2009;19:4973-4980.